The Influence of Midlevel Shear and Horizontal Rotors on Supercell Updraft Dynamics

ANDREW J. MUEHR,[a,b,c] JAMES H. RUPPERT,[a] MATTHEW D. FLOURNOY,[d,a,c] AND JOHN M. PETERS[e]

[a] School of Meteorology, University of Oklahoma, Norman, Oklahoma
[b] Cooperative Institute for Severe and High-Impact Weather Research and Operations, Norman, Oklahoma
[c] NOAA/OAR/National Severe Storms Laboratory, Norman, Oklahoma
[d] NOAA/NWS/NCEP/Storm Prediction Center, Norman, Oklahoma
[e] Department of Meteorology and Atmospheric Science, The Pennsylvania State University, University Park, Pennsylvania

(Manuscript received 2 May 2023, in final form 7 November 2023, accepted 8 November 2023)

ABSTRACT: Large midlevel (3–6 km AGL) shear is commonly observed in supercell environments. However, any possible influence of midlevel shear on an updraft has been relatively unexplored until now. To investigate, we ran 10 simulations of supercells in a range of environments with varying midlevel shear magnitudes. In most cases, larger midlevel shear results in a storm motion that is faster relative to the low-level hodograph, meaning that larger midlevel shear leads to stronger low-level storm-relative flow. Because they are physically connected, we present an analysis of the effects of both midlevel shear and low-level storm-relative flow on supercell updraft dynamics. Larger midlevel shear does not lead to an increase in cohesive updraft rotation. The tilting of midlevel environmental vorticity does lead to localized areas of larger vertical vorticity on the southern edge of the updraft, but any dynamical influence of this is overshadowed by that of much larger horizontal vorticity in the same area associated with rotor-like circulations. This storm-generated horizontal vorticity is the primary driver behind lower nonlinear dynamic pressure on the southern flank of the midlevel updraft when midlevel shear and low-level storm-relative flow are larger, which leads to a larger nonlinear dynamic pressure acceleration in those cases. Storm-generated horizontal vorticity is responsible for the lowest nonlinear dynamic pressure anywhere in the midlevel updraft, unless the mesocyclone becomes particularly intense. These results clarify the influence of midlevel shear on a supercell thunderstorm, and provide additional insight on the role of low-level storm-relative flow on updraft dynamics.

SIGNIFICANCE STATEMENT: Persistent rotation in supercell thunderstorms results from the tilting of horizontal spin into the vertical direction. This initially horizontal spin is the result of shear, which is a change in wind speed and/or direction with height. More shear in the layer 0–3 km above ground level is well understood to lead to stronger rotation within the storm, but the influence of shear in the 3–6-km layer is unclear and is investigated here. We find that horizontal spin originating in the 3–6-km layer has little impact on vertically oriented thunderstorm rotation. Instead, intense regions of horizontal spin that are generated by the storm itself (rather than having originated from the background environment) dominate storm dynamics at midlevels.

KEYWORDS: Updrafts/downdrafts; Wind shear; Mesocyclones; Severe storms; Supercells

1. Introduction

The collocation of positive vertical velocity (w) and vertical vorticity (ζ) in a supercell is known as a "mesocyclone," and has been a primary focus of supercell research for several decades (Browning 1964; Davies-Jones 1984, 2002; Rotunno and Klemp 1982, 1985; Markowski and Richardson 2014; Dahl 2017). The low-level mesocyclone is of significant interest, due to its connection with tornadoes (Adlerman et al. 1999; Coffer et al. 2017; Murdzek et al. 2020; Flournoy et al. 2020; Peters et al. 2023), and the strength of low-level mesocyclone rotation has an established connection to low-level preexisting environmental and baroclinic horizontal vorticity (ω_h; Klemp and Rotunno 1983; Davies-Jones 1984, 2022; Rotunno and Klemp 1985; Dahl et al. 2014; Dahl 2015; Coffer and Parker 2015; Peters et al. 2020b; Goldacker and Parker 2021; hereafter, "preexisting environmental horizontal vorticity" is referred to as simply "environmental vorticity"). While the tilting of low-level (i.e., 0–3 km AGL) environmental vorticity associated with the background vertical wind shear is understood to result in the development and maintenance of the midlevel mesocyclone (Rotunno 1981; Rotunno and Klemp 1982; Davies-Jones 1984), the influence of environmental vorticity at midlevels (e.g., 3–6 km AGL) on the midlevel mesocyclone is less understood.

The potential importance of vertical wind shear at midlevels (hereafter "midlevel shear") is heightened by the fact that vorticity within the midlevel mesocyclone plays a role in determining vertical pressure gradient accelerations, which are known to influence the strength of the updraft (Rotunno and Klemp 1982; Brandes 1984; McCaul and Weisman 1996; Weisman and Rotunno 2000; Goldacker and Parker 2021). Several studies have found that alignment of the midlevel mesocyclone with the low-level mesocyclone is necessary for low-level updraft intensification (Dowell and Bluestein 2002; Skinner et al. 2014; Marquis et al. 2016; Guarriello et al. 2018; Brown and Nowotarski 2019). Peters et al. (2020b) noted that most air participating in updraft vertical vorticity maxima at

---

Corresponding author: Andrew Muehr, andrew.muehr@noaa.gov

DOI: 10.1175/JAS-D-23-0082.1

© 2024 American Meteorological Society. This published article is licensed under the terms of the default AMS reuse license. For information regarding reuse of this content and general copyright information, consult the AMS Copyright Policy (www.ametsoc.org/PUBSReuseLicenses).

Brought to you by NOAA Library | Unauthenticated | Downloaded 04/01/25 02:50 PM UTC

4–8 km AGL originated from above 2 km AGL, suggesting that tilted environmental vorticity originating from levels higher than often studied plays a nonnegligible role in the midlevel mesocyclone and associated low pressure. Motivated by these issues, in this study we examine the influences of midlevel environmental vorticity on supercell updrafts and characteristics.

Unlike at low levels, midlevel environmental vorticity exists in a layer that typically has no convective available potential energy (CAPE). Thompson et al. (2007) defined the conditionally unstable layer that provides the vast majority of parcels participating in the updraft core (Nowotarski et al. 2020) as the "effective inflow layer" (EIL), which is typically contained below 3 km. To evaluate the effect of midlevel environmental vorticity on a supercell's updraft, we must consider the entrainment of above-EIL air, which, by definition, has less CAPE than EIL air.

The effects of entrainment have been a focal point of studies on cumulus parameterization and tropical convection for decades (Emanuel 1991; Lin and Arakawa 1997a,b; Zipser 2003; Romps and Kuang 2010; de Rooy et al. 2013; Morrison 2016a,b, 2017). In the severe storms community, the effects of entrainment on precipitation intensity, appearance, and hazards of severe thunderstorms have been examined in many previous studies (Bluestein and Parks 1983; Bluestein and Woodall 1990; Gilmore and Wicker 1998; James and Markowski 2010; Grant and van den Heever 2014), but have only been rigorously applied to severe thunderstorm updraft thermodynamics in recent years (Peters et al. 2019, 2020b,c, 2022a,b,c; Lasher-Trapp et al. 2021; Jo and Lasher-Trapp 2022, 2023; Mulholland et al. 2021). These previous studies have primarily focused on the thermodynamic effect of entrainment, which entails a reduction of buoyancy and precipitation efficiency. While increased shear results in greater wake entrainment at early stages (LeBel and Markowski 2023), supercell updrafts usually become wide enough to resist any deleterious effects. Any kinematic influence of entrained vorticity-rich air during the mature stage remains ambiguous, and observed supercell proximity soundings often show large shear and associated environmental vorticity in the middle troposphere (Maddox 1976; Parker 2014; Coniglio and Parker 2020). While the entrainment of midlevel air is locally detrimental to the buoyancy of an updraft, tilted midlevel environmental vorticity could enhance the pressure perturbation associated with the midlevel mesocyclone, ultimately increasing updraft strength. Therefore, we will examine the following hypothesis: *Increasing midlevel shear enhances the midlevel mesocyclone.*

To examine this hypothesis, an intuitive first step would be to consider the relationship between updraft vertical vorticity and midlevel shear (MLS; for simplicity, we treat MLS as a time-independent, fixed environmental parameter herein). However, compared to an environment with small MLS, an environment with large MLS (and midlevel environmental vorticity) requires faster mid- and upper-level winds, resulting in a faster storm motion relative to the low-level hodograph. Therefore, any influence of MLS and tilted environmental vorticity on a mesocyclone could be conflated with influences from altered storm-relative variables. The effect of increasing MLS on storm-relative variables becomes apparent when considering a vertical shear profile representative of observed Northern Hemisphere supercell events, where shear is predominantly southerly below 1 km and veers to attain a larger westerly component above 1 km (Maddox 1976; Davies-Jones 1984; Parker 2014; Coniglio and Parker 2020). In such a vertical shear profile, increasing westerly shear above 1 km results in a storm motion that is more removed from the low-level hodograph (i.e., lowest 0–1 km AGL), meaning that low-level storm-relative flow (LL SR flow) has increased. This relationship is visible in Fig. 1, discussed in detail in section 2, and is borne out in the idealized simulations of Brooks et al. (1994), Warren et al. (2017), and Peters et al. (2019), where increasing deep-layer shear results in larger LL SR flow, which has an established relationship with supercell updrafts.

Davies-Jones (1984) and Droegemeier et al. (1993) noted that LL SR flow must exceed a threshold for supercell maintenance, often around 10 m s^{-1}. Warren et al. (2017) found that simulated supercell updrafts grew wider as LL SR flow increased, resulting in larger vertical mass flux and hydrometeor production. Peters et al. (2019) affirmed this relationship, demonstrating that increased updraft width (a product of increased mass flux via increased LL SR flow and inflow) leads to updraft cores that are more sheltered from entrained air, and these less-diluted updraft cores have larger buoyancy (Morrison 2017; Morrison et al. 2020; Peters et al. 2020c). The decreased interaction of entrained midlevel air with the cores of wider updrafts is a focal point of our analysis, since this implies that the cores of wider updrafts have little interaction with midlevel environmental vorticity. Furthermore, updraft width has been connected to downdraft size and buoyancy perturbations in cold pools (Marion and Trapp 2019) and off-hodograph propagation (Davies-Jones 2002).

Given the structure of a typical supercell-supportive hodograph, an increase in MLS results in an increase in both midlevel environmental vorticity and LL SR flow (Fig. 1). These two variables are physically connected, and holding LL SR flow constant while MLS increases would require changing shear over other layers (and unrealistic hodographs). Therefore, we intentionally do not perform an experiment where the effect of MLS is isolated. Assuming that the effect of tilted midlevel environmental vorticity is generally similar to that of low-level environmental vorticity (i.e., locally large vertical vorticity), increasing MLS, by virtue of its connection with LL SR flow, will lead to multiple distinct influences on supercell characteristics. LL SR flow exerts a large control on updraft width, while midlevel shear likely influences updraft rotation. To thoroughly evaluate the influence of MLS on supercells, the unique influences of each variable must be examined. Therefore, in this study we address two questions:

1) How does tilted midlevel environmental vorticity influence a supercell mesocyclone?
2) How does low-level storm-relative flow modulate the updraft and influence of tilted midlevel environmental vorticity?

Brought to you by NOAA Library | Unauthenticated | Downloaded 04/01/25 02:50 PM UTC

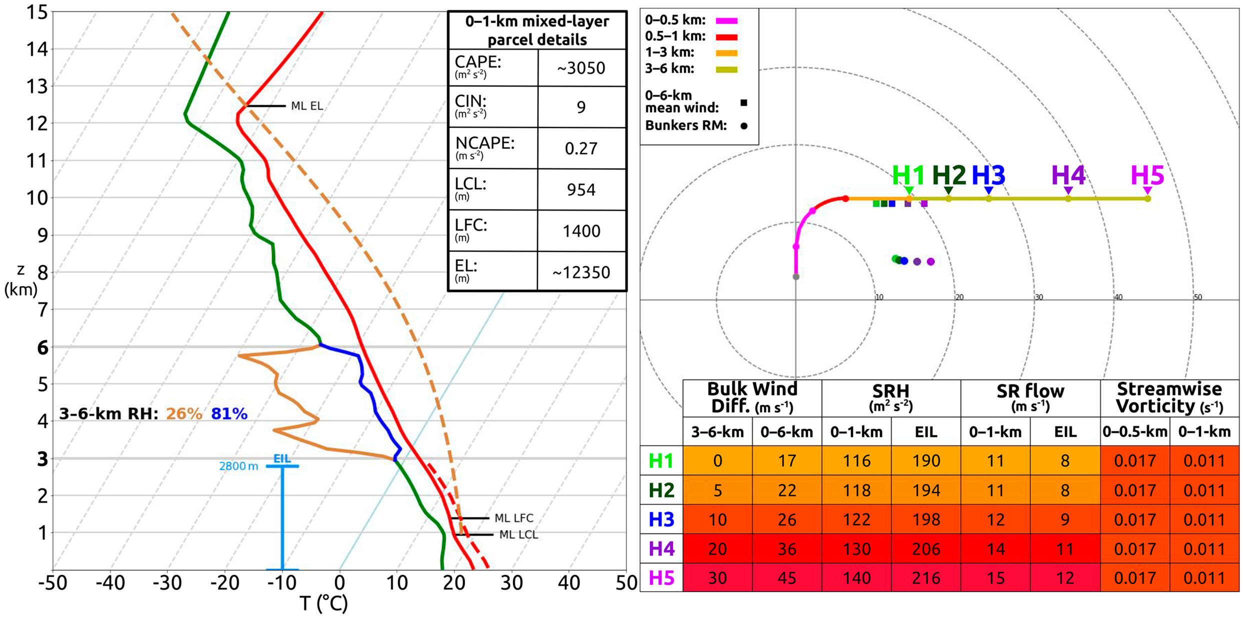

0–1-km mixed-layer parcel details	
CAPE: ($m^2\ s^{-2}$)	~3050
CIN: ($m^2\ s^{-2}$)	9
NCAPE: ($m\ s^{-2}$)	0.27
LCL: (m)	954
LFC: (m)	1400
EL: (m)	~12350

	Bulk Wind Diff. ($m\ s^{-1}$)		SRH ($m^2\ s^{-2}$)		SR flow ($m\ s^{-1}$)		Streamwise Vorticity (s^{-1})	
	3–6-km	0–6-km	0–1-km	EIL	0–1-km	EIL	0–0.5-km	0–1-km
H1	0	17	116	190	11	8	0.017	0.011
H2	5	22	118	194	11	8	0.017	0.011
H3	10	26	122	198	12	9	0.017	0.011
H4	20	36	130	206	14	11	0.017	0.011
H5	30	45	140	216	15	12	0.017	0.011

FIG. 1. Hodograph and skew *T*. The H1–H5 labels demarcate the 6-km wind for each respective hodograph. The first fuchsia dot on the hodograph indicates the 250-m wind, where clockwise curvature with height begins. All storm-relative calculations use the Bunkers RM motion. The dashed red line indicates virtual temperature. NCAPE is the CAPE divided by the depth between the LFC and EL. Hodograph rings are every 10 m s^{-1}.

Output from a matrix of simulated supercells is used to address these questions. In addition to differences between simulated supercells caused by variations in MLS and LL SR flow, we find regions of large storm-generated horizontal vorticity at midlevels that play a role in updraft dynamics. These findings are discussed in detail.

2. Methods

a. Model details

To answer our questions, we ran and investigated a matrix of 10 simulated supercells in environments with varied MLS and relative humidity (RH). All simulations were performed using Cloud Model 1 (CM1; Bryan and Fritsch 2002) version 21.0. Storms were simulated within a 120 km × 120 km × 18.5 km storm-following domain, with 250-m horizontal grid spacing and constant 100-m vertical grid spacing, a grid capable of sufficiently resolving finescale, turbulent convective processes (Lebo and Morrison 2015). The lowest model level was 50 m. The upper and lower boundary conditions were free slip, and lateral boundary conditions were open radiative. Rayleigh damping was applied above 15 km. Morrison double-moment microphysics (Morrison et al. 2009) were used, simulations were run for three hours, and data files were saved every five minutes. A warm bubble (Klemp and Wilhelmson 1978) was used to initiate convection, with a +5-K temperature perturbation and depth of 1400 m, similar to Parker (2017), but with a width of 10 km. The namelist.input file and model soundings can be accessed through the repository linked in the data availability statement.

b. Choosing the thermodynamic profile and hodograph

We used two modified versions of the VORTEX-2 composite, tornadic near-field thermodynamic profile (Parker 2014) for our simulations (Fig. 1). One profile contains high 3–6-km RH (81%, layer averaged), and the other contains low 3–6-km RH (26%, layer averaged). Several test runs proved warm bubble convection initiation (CI) to be exceedingly difficult in the unmodified VORTEX-2 thermodynamic profile due to dry air. To facilitate CI, the 0–1-km mixing ratio was increased by 1 g kg^{-1} relative to the original sounding, and we nonuniformly increased the mixing ratio in the 1–3-km layer through a process of trial and error. These two modifications facilitated warm bubble CI and storm maintenance, even in the presence of the added midlevel dry layer. Low free-tropospheric RH is known to be detrimental to updraft buoyancy, particularly when updrafts are narrow (Morrison 2017). In contrast, high free-tropospheric RH can support updrafts at even very narrow widths (Morrison et al. 2020, 2022; Peters et al. 2020c, 2022b,c). For our purposes, midlevel RH was varied as an experimental parameter to influence the dilution of the updraft core by entrained midlevel air and characterize how this impacts its interaction with the associated vorticity.

The vertical wind profile is based on the Rotunno and Klemp (1982) quarter-circle hodograph but is modified to better represent observed hodographs in supercell events, primarily those in the Great Plains during spring (Fig. 1; e.g., Coniglio and Parker 2020; Parker 2014; Maddox 1976). All curvature is concentrated below 1 km, but above a layer of unidirectional, southerly shear from 0 to 250 m, as in the composite supercell sounding of Coniglio and Parker (2020). The

Brought to you by NOAA Library | Unauthenticated | Downloaded 04/01/25 02:50 PM UTC

0–3-km segments of each hodograph are identical for each ensemble member, with shear and ground-relative wind speeds roughly consistent with the values of the dataset in Coniglio and Parker (2020). There is no shear above 6 km in any simulation as the wind is held constant at its 6-km value.

MLS (henceforth referring to bulk wind difference the 3–6-km layer) is westerly and unidirectional in all simulations, and increases from 0 to 30 m s^{-1} driving an increase in 3–6-km environmental vorticity from 0 to 0.01 s^{-1} across five unique hodographs (H1–H5). As MLS increases, the storm motion increases relative to the low-level hodograph, increasing LL SR flow, akin to Brooks et al. (1994) and Warren et al. (2017). Using the storm motion predicted by the method in Bunkers et al. (2000, 2014), the 0–0.5- and 0–1-km streamwise vorticity magnitude is held nearly constant; the largest difference between any two hodographs is less than 5%. Low-level storm-relative helicity (SRH; Lilly 1986a,b; Davies-Jones et al. 1990) increases incrementally between H1 and H5, but is driven only by an increase in LL SR flow, not streamwise vorticity. The only layer where environmental vorticity changes across simulations is the midlevels, lending confidence that any rotational differences between simulated updrafts are the result of variations in MLS, LL SR flow, or stochastic internal storm processes (Coffer et al. 2017; Flournoy et al. 2020; Markowski 2020; Lyza et al. 2022). Two different thermodynamic profiles and five different hodographs resulted in a suite of 10 simulations driven from unique initial model profiles, the output of which is analyzed in the following section. Individual members are referred to by their hodograph (e.g., H2) and midlevel RH value (e.g., "dry" or "moist").

Many previous supercell modeling studies have focused on tornadogenesis in environments characterized by high-end values of shear and SRH (Klemp and Rotunno 1983; Wicker and Wilhelmson 1995; Schenkman et al. 2014; Orf et al. 2017; Coffer and Parker 2017; Flournoy et al. 2020). To better represent environments associated with the majority of supercells, which tend to be nontornadic (Trapp et al. 2005), our hodographs contain values of low-level shear and SRH that fall within the middle 50% of nontornadic or weakly tornadic supercell environments in large datasets of modeled and observed proximity soundings (Rasmussen and Blanchard 1998; Thompson et al. 2007; Nixon and Allen 2022), and are similar to the two most common hodographs from Warren et al. (2021, see their Figs. 4 and 6).

c. *Diagnosing dynamical contributions to vertical velocity*

Given that the main focus of this study is how MLS and LL SR flow influence vorticity within an updraft and how this modulates updraft dynamics, we consider the nonlinear dynamic pressure perturbations caused by vorticity (or deformation), in addition to linear dynamic and buoyancy pressure perturbations. The buoyant (p'_B), linear dynamic (p'_L), and nonlinear dynamic (p'_{NL}) contributions to the pressure perturbation field are computed using the methodology of Hastings and Richardson (2016) and expressed here as

$$\nabla^2 p'_B = \frac{\partial(\rho_0 B)}{\partial z},$$

$$\nabla^2 p'_L = -\rho_0 \nabla w \cdot \frac{dV_0}{dz}, \quad \text{and}$$

$$\nabla^2 p'_{\mathrm{NL}} = -\rho_0\left(e'_{i,j}e'_{i,j} - w^2\frac{d^2\ln\rho_0}{dz^2} - \frac{\boldsymbol{\omega}'\cdot\boldsymbol{\omega}'}{2}\right), \qquad (1)$$

where $\rho_0(z)$ is the density from the initial model sounding, V_0 is the horizontal wind from the initial model sounding, $e'_{i,j} \equiv (\partial v'_i/\partial x_j + \partial v'_j/\partial x_i)$ is the rate-of-deformation tensor of the storm-modified wind v'_i, $\boldsymbol{\omega}'$ is the vector vorticity of the storm-modified wind, and $B = g(\theta'/\theta_0) + gq'_v(R_d/R_v - 1) - g(q_c)$ is the CM1 approximation of buoyancy [where g is the gravitational acceleration, θ' and θ_0 are the potential temperature perturbation and potential temperature base states (respectively), q'_v is water vapor mixing ratio perturbation, R_d and R_v are the gas constants for dry and wet air (respectively), and q_c is condensate]. Assuming that $\nabla^2 p' \propto -p'$ (Markowski and Richardson 2010), which is generally true for well-behaved fields away from the domain boundaries, these calculations can be used to at least qualitatively describe local accelerations (Rotunno and Klemp 1982; Rotunno and Weisman 2003), particularly at midlevels (Davies-Jones 2002, his Fig. 6), where our analysis is focused.

From Eq. (1), p'_{NL} will be positive where flow deformation is large (i.e., locally high nonlinear dynamic pressure) and negative where storm-modified vorticity $\boldsymbol{\omega}'$ is large in magnitude (i.e., locally low nonlinear dynamic pressure). Our analysis focuses heavily on p'_{NL} and, to a lesser extent, p'_L because of their dependence on storm-modified vorticity and the interaction of the environmental wind shear with the updraft, respectively.

To assess the influence of dynamical and buoyant effects on updraft speed from the terms in Eq. (1), we analyze vertical accelerations from each term in the anelastic inviscid vertical momentum equation (Parker and Johnson 2004) expressed here as in Peters et al. (2020b):

$$\frac{Dw}{Dt} = B - \frac{1}{\rho_0}\frac{\partial p'_B}{\partial z} - \frac{1}{\rho_0}\frac{\partial p'_L}{\partial z} - \frac{1}{\rho_0}\frac{\partial p'_{\mathrm{NL}}}{\partial z}. \qquad (2)$$

Previous work has shown that supercell updrafts are influenced by each term of Eq. (2). Updraft width, connected to LL SR flow and positively correlated with deep-layer shear, modifies the influences of buoyancy [B; first term on the rhs of Eq. (2); Peters et al. 2019] and the buoyancy pressure acceleration [BPA; second term on the rhs of Eq. (2)] term [which sum to the effective buoyancy pressure acceleration (EBPA); Davies-Jones 2003]. The linear dynamic pressure acceleration [LDPA; third term on the rhs of Eq. (2)] and the nonlinear dynamic pressure acceleration [NLDPA; fourth term on rhs of Eq. (2)] are dependent on the vertical gradient in p'_L and p'_{NL}, respectively. Since p'_{NL} is dependent on storm-modified vorticity ($\boldsymbol{\omega}'$), and p'_L is dependent on the interaction of environmental wind shear with the updraft (Rotunno and Klemp 1982; Davies-Jones 1984, 2002), this means NLDPA and LDPA, the

Brought to you by NOAA Library | Unauthenticated | Downloaded 04/01/25 02:50 PM UTC

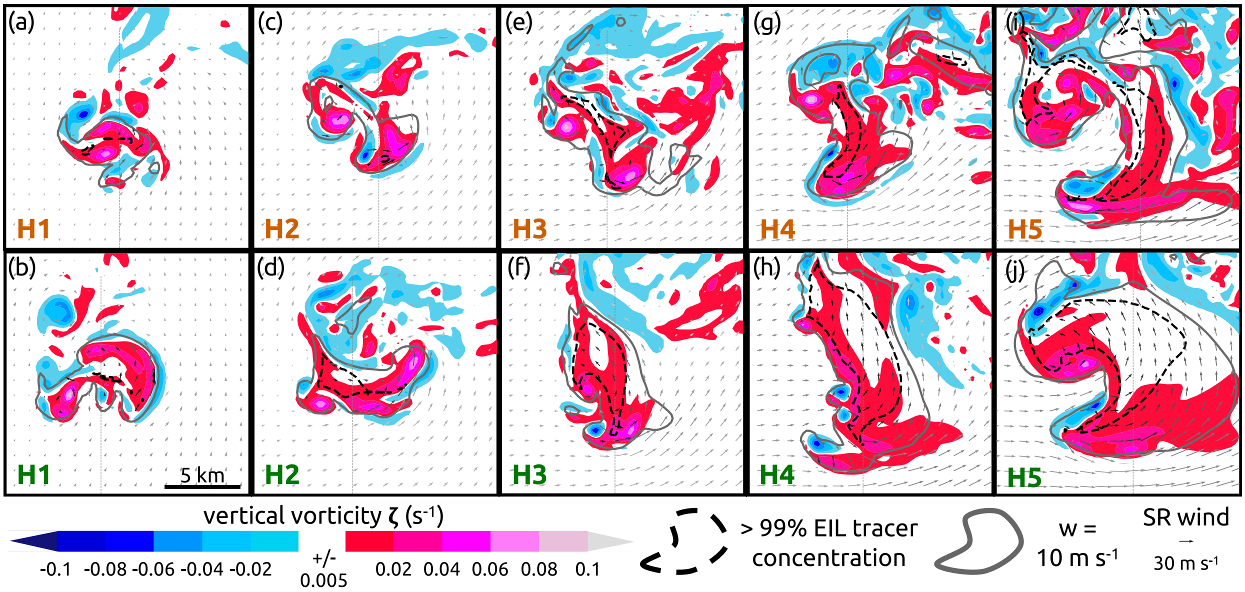

FIG. 2. 16 × 16 km^2 plan views for each storm at 6 km AGL, displayed at the time of maximum 6-km rotational velocity for each storm within the t = 1–2-h period, showing vertical vorticity (red to blue fill), where vertical velocity equals 10 m s^{-1} (gray contour), the outline of where EIL tracer concentration exceeds 99% (dashed black contour), and storm-relative winds (vectors, plotted every 1 km with darker vectors indicating larger vertical velocity). (a),(c),(e),(g),(i) Simulations where midlevel RH is low are denoted by brown text, and (b),(d),(f),(h),(j) simulations where midlevel RH is high are denoted by green text.

terms dependent on the vertical distribution of p'_{NL} and p'_L, respectively, are the terms in Eq. (2) that best reflect dynamical effects on vertical velocity as a result of vorticity within supercell updrafts and varied MLS (McCaul and Weisman 1996; Goldacker and Parker 2021). Accordingly, these terms are the most relevant in our forthcoming analysis.

d. Updraft tracking, time averages, and tracers

To assess general updraft characteristics, we analyze several time-averaged variables. We define the center of the updraft as the centroid of all locations where vertical velocity exceeds the 75th-percentile value of all 3–6-km layer-averaged vertical velocity values larger than 5 m s^{-1} within the right-moving storm, similar to the method used by Warren et al. (2017). Several other methods for tracking the updraft center were tested, but this method produced time-averaged data that best reflected trends and features across manually inspected individual time steps. All time-averaged plots consist of data from each time step centered on this updraft center point and averaged over the corresponding length of time, but most plan views and cross sections display data at a single time step so that the clarity of finescale, often brief processes is preserved. General updraft metrics (e.g., rotational velocity) are computed for each time step and then divided by the corresponding length of time.

At t = 0 min, passive tracers were initialized from 0 to 2.5 km (~90% of EIL depth) and 3–6 km AGL (midlevels), allowing us to isolate regions where midlevel air has mixed with CAPE-rich air originating from the EIL, and where EIL air has ascended through the midlevels without dilution. This allows us to separate the updraft into regions that have and have not been influenced by entrained midlevel air and the associated environmental vorticity.

3. Results

a. How does tilted midlevel environmental vorticity influence the midlevel mesocyclone?

Each of the 10 simulations contain discrete, right-moving supercells exhibiting continuous regions of mesocyclone-strength vertical vorticity [>0.005 s^{-1}; the threshold used by Davies-Jones (1984) to define a mesocyclone] extending throughout several kilometers of the updraft (a view of the midlevel mesocyclones is provided in Fig. 2). Our mentions of "midlevel mesocyclone" primarily refer to the region of generally positive vertical vorticity contained within undiluted EIL air at midlevels, where the tilting of low-level environmental vorticity is commonly understood to result in rotation (e.g., Rotunno and Klemp 1982; Davies-Jones 1984). These supercells persist through at least t = 120 min, after which the simulated storms in the H1 and H2 environments weaken considerably. Therefore, our analysis focuses primarily on the t = 1–2-h period.

At 6 km AGL, vertical vorticity maxima in each storm occur where EIL air has mixed with entrained above-EIL air (i.e., outside of the >99% EIL tracer concentration contour, Fig. 2), suggesting that the tilting of midlevel environmental vorticity may contribute to local maxima in vertical vorticity. This is corroborated by the simulations of Peters et al. (2020b, their Figs. 17c,d) and the radar observations of Cai and Wakimoto (2001, their Fig. 11a), who found large vertical vorticity at the edge of the midlevel updraft in environments with large MLS.

Brought to you by NOAA Library | Unauthenticated | Downloaded 04/01/25 02:50 PM UTC

However, the largest values of vertical vorticity actually occur within the diluted midlevel updraft in the H2-moist case (Fig. 2d), even though MLS is small (as well as in the other H2 and H1 cases, but the extent of undiluted EIL air at 6 km is very small in those updrafts). Furthermore, pronounced vertical vorticity minima often occur near the maxima, and in some cases are larger in magnitude than any nearby positive vertical vorticity.

These results warrant a more objective analysis of mesocyclone strength within the 10 simulations. To do this, we analyze trends in rotational velocity [calculated as $A\bar{\zeta}/(2\pi^{1/2}A^{1/2})$, where A is updraft area and $\bar{\zeta}$ is the average vorticity of the updraft, as in Peters et al. (2023)]: a measure of cohesive updraft rotation that is connected to the rotation-induced pressure deficit within a mesocyclone and routinely used to assess mesocyclone strength (Gibbs and Bowers 2019; Bentley et al. 2021; Peters et al. 2023). There is no statistically significant trend in 6-km rotational velocity within the updraft (i.e., where vertical velocity exceeds 10 m s^{-1}) as MLS increases (Fig. 3a). This suggests that an increase in midlevel environmental vorticity does not lead to an increase in cohesive updraft rotation. However, where the 6-km updraft only contains undiluted EIL air, rotational velocity exhibits a positive trend with MLS that is significant at the 99% confidence level using the Pearson correlation coefficient (Fig. 3b). Since this air has had no interaction with midlevel air, and therefore is not directly influenced by midlevel environmental vorticity, this suggests that the trends in rotational velocity are the result of an indirect influence of MLS on updraft characteristics related to LL SR flow. The undiluted regions in the H1-dry, H1-moist, and H2-dry updrafts (Figs. 2a–c, which experience the weakest LL SR flow) are very small, which likely reduces the utility of rotational velocity calculations for these regions. Omitting these three simulations results in no statistical significance for the trend in rotational velocity as MLS increases using both the Spearman rank and Pearson methods. Regardless, any of the weak positive correlation between midlevel rotational velocity and MLS in Fig. 3a appears to be driven by trends within the undiluted updraft.

Within the region of the 6-km updraft that has mixed with midlevel air, and therefore is directly influenced by MLS, there is a weak negative correlation between MLS and rotational velocity (Fig. 3c). This continues to indicate that increasing MLS does not lead to an increase in cohesive updraft rotation. Even without considering the particularly weak rotational velocities of the diluted H5 updraft regions, there is no trend in rotational velocity across the simulations, despite a 20 m s^{-1} difference in MLS. When averaging variables over the 3–6-km layer, each of the results presented in Fig. 3 hold true.

While Fig. 3 suggests that increasing midlevel environmental vorticity does not lead to increased updraft rotation, the presence of vertical vorticity maxima outside of the undiluted EIL air in Fig. 2 suggests perhaps a more localized influence of MLS. To investigate this, we analyze vertical cross sections passing south to north through the midlevel updraft (Fig. 4) along the paths plotted in Fig. 2. The tilting of midlevel environmental vorticity is indicated by hatched regions within the dashed black contour on the south (left) side of the midlevel updraft. In each of the H4 and H5 simulations (Figs. 4g–j), local

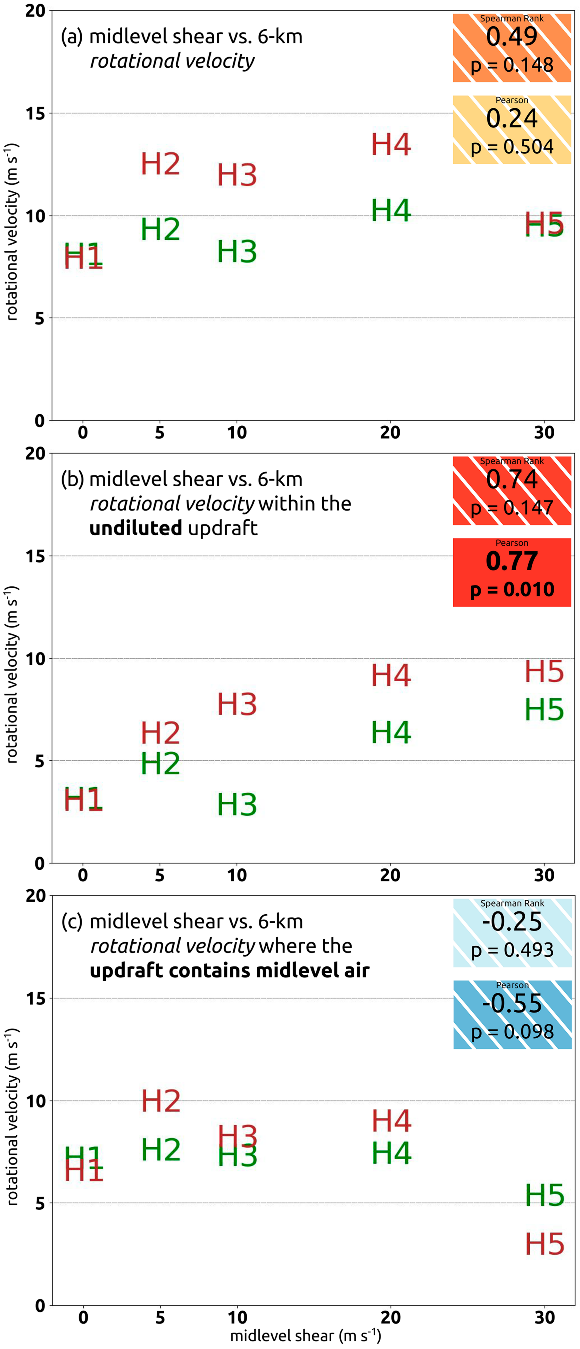

FIG. 3. Midlevel shear vs 6-km rotational velocity, averaged over the t = 1–2-h period, (a) within the entire updraft (where w exceeds 10 m s^{-1}), (b) within the part of the updraft where EIL tracer concentration exceeds 99%, and (c) within the part of the updraft where midlevel tracer concentration exceeds 1%. The Pearson and Spearman rank correlation coefficients and p values are displayed on the right side of each plot, with boldface text atop an unhatched background indicating statistical significance. Warm colors behind the values indicate positive correlation coefficients, with values closer to 1 appearing atop red backgrounds, and cool colors behind the values indicate negative correlation coefficients, with values closer to −1 appearing atop dark blue backgrounds.

Brought to you by NOAA Library | Unauthenticated | Downloaded 04/01/25 02:50 PM UTC

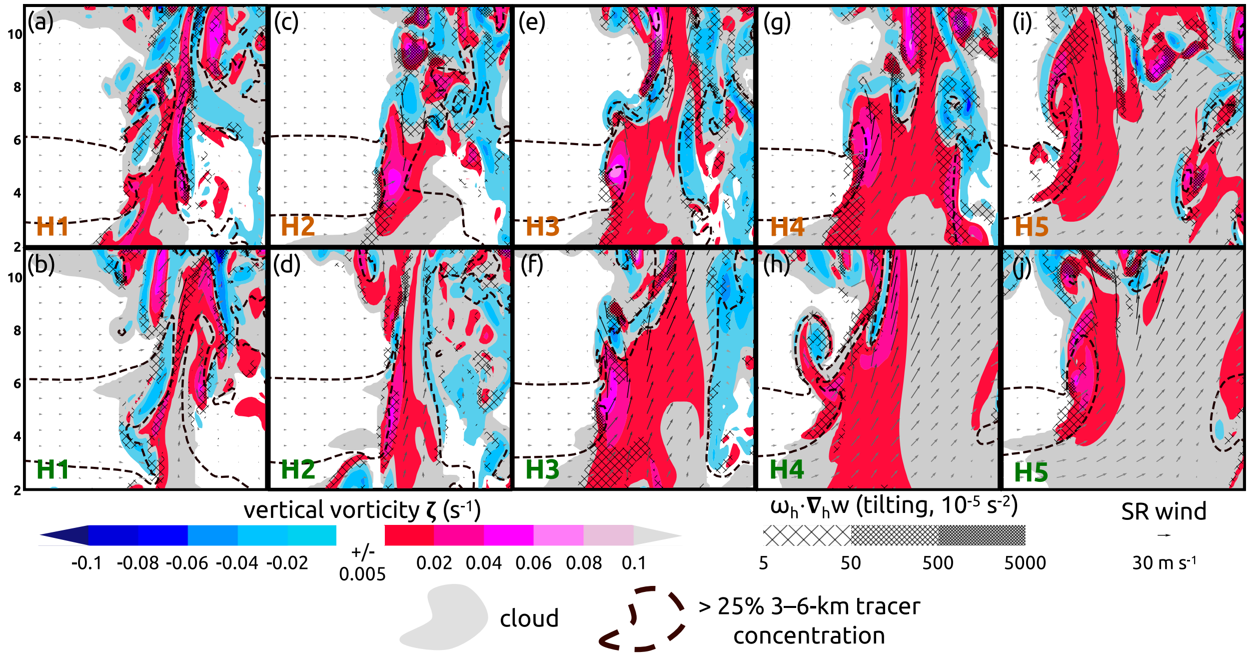

FIG. 4. South-to-north (left to right in each panel) vertical cross sections through each updraft at its time of maximum 6-km rotational velocity during the $t = 1$–2-h period along the paths in Fig. 2. The cross sections extend 18 km in the y direction and 9 km in the z direction (z-axis labels in km). Shown is vertical vorticity as in Fig. 2, tilting (black hatching), cloud ($q_i + q_c > 0.0001$ g kg^{-1}; gray fill), the outline of where 3–6-km tracer concentration exceeds 25% (dashed black contours), and storm-relative wind vectors plotted every 1500 m in the horizontal and 600 m in the vertical, with darker vectors indicating larger vertical velocity.

vertical vorticity maxima of 0.02–0.05 s^{-1} can be found where midlevel tracer concentration exceeds 25% in the vicinity of positive tilting, indicating that the tilting of midlevel environmental vorticity is at least partially contributing to a local increase in vertical vorticity on the southern edge of the updraft. This signal is less evident in the H1 and H2 simulations (Figs. 4a–d); the largest values of vertical vorticity tend to reside outside of the midlevel air. The vertical vorticity pattern in those updrafts, however, tends to be more complicated and difficult to interpret, perhaps indicative of a thermal chain-like structure characteristic of narrower updrafts (e.g., Peters et al. 2020c).

Tilted midlevel environmental vorticity contributes to local maxima in vertical vorticity at the southern edge of the midlevel updraft (Fig. 4). However, horizontal vorticity maxima in this same part of the updraft tend to be 2–4 times larger than any nearby vertical vorticity (Fig. 5). As a result, $p'_{\rm NL}$ minima at midlevels are more strongly tied to horizontal vorticity maxima (Fig. 5) than vertical vorticity extrema, since the fluid shear term of $p'_{\rm NL}$ [Eq. (1)] is proportional to the square of storm-modified vorticity. Note that above 3 km, any vorticity in the x direction represents storm-modified vorticity, since all preexisting environmental vorticity is in the y direction. The regions of horizontal vorticity in Fig. 5 generally take on a more concentrated, rounded appearance from H1 to H5, with the $p'_{\rm NL}$ minima decreasing as well. Of course, vertical vorticity still contributes to the local $p'_{\rm NL}$ minima, but Fig. 5 suggests that horizontal vorticity is the primary driver of low $p'_{\rm NL}$ at midlevels at $t = 1$–2 h in the simulations.

Figure 6 shows $p'_{\rm NL}$ on the order of -1 hPa throughout portions of each midlevel updraft, with the most intense $p'_{\rm NL}$ minima at 6 km reaching less than -6 hPa and occurring near the southern edge of the updraft [as in Cai and Wakimoto (2001) and Peters et al. (2020b)] in all but the H1 cases. Horizontal vorticity regularly exceeds 0.06–0.1 s^{-1} in the vicinity of these $p'_{\rm NL}$ minima. Save for highly localized extrema, vertical vorticity is often less than 0.04 s^{-1} in the vicinity of the most intense $p'_{\rm NL}$ minima, continuing to suggest that horizontal vorticity drives nonlinear dynamics at midlevels. Vertical vorticity extrema that exist outside of large horizontal vorticity still result in local $p'_{\rm NL}$ minima, but these are much smaller in magnitude than those occurring in the vicinity of horizontal vorticity maxima, except in the H1 cases. Additionally, in almost every instance where both horizontal vorticity and $p'_{\rm NL}$ are large in magnitude, there exists a local maximum in vertical vorticity (Fig. 6). These relationships are examined in detail shortly. Given that horizontal vorticity is generally larger in magnitude and more collocated with $p'_{\rm NL}$ minima than vertical vorticity, the remainder of this section focuses primarily on the influence of storm-generated horizontal vorticity on updraft characteristics and dynamics.

b. *The formation and characteristics of horizontal rotors*

Horizontal, toroidal circulations have long been observed and known to influence the dynamics of real and idealized cumulus clouds (Hill 1894; Damiani and Vali 2007; Morrison and Peters 2018). However, the shear in supercell environments substantially modifies updrafts from their initial cumuliform

Brought to you by NOAA Library | Unauthenticated | Downloaded 04/01/25 02:50 PM UTC

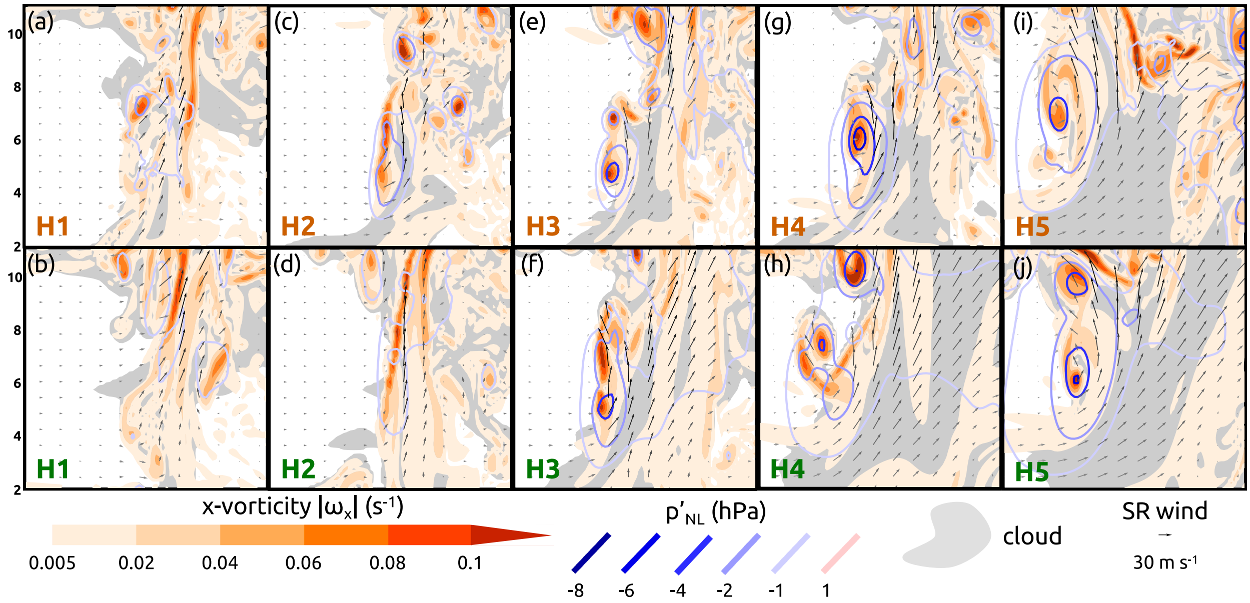

FIG. 5. As in Fig. 4, but showing positive x-direction horizontal vorticity (orange fill) and nonlinear dynamic pressure perturbation (blue to red contours). The tracer concentration contour is omitted in this figure.

stages. After Rotunno and Klemp (1982, 147–148, 1985) suggested that baroclinically generated horizontal vortex rings around the updraft could substantially contribute to storm splitting, Cai and Wakimoto (2001) observed and described these regions of large horizontal vorticity (as depicted in Fig. 5) in terms of their relationship to a supercell updraft. In their radar analysis, they noted that large horizontal vorticity developed at the edge of the midlevel updraft due to a horizontal gradient in buoyancy (see their Fig. 11f). This baroclinically generated horizontal vorticity is also discussed by Lasher-Trapp et al. (2021) and Jo and Lasher-Trapp (2022, 2023). In their analyses of entrainment in a simulated supercell thunderstorm, they described persistent “ribbon-like features” of horizontal vorticity that formed along the horizontal buoyancy gradient at the updraft edge and gradually ascended along the southern edge of the updraft. Our analysis affirms

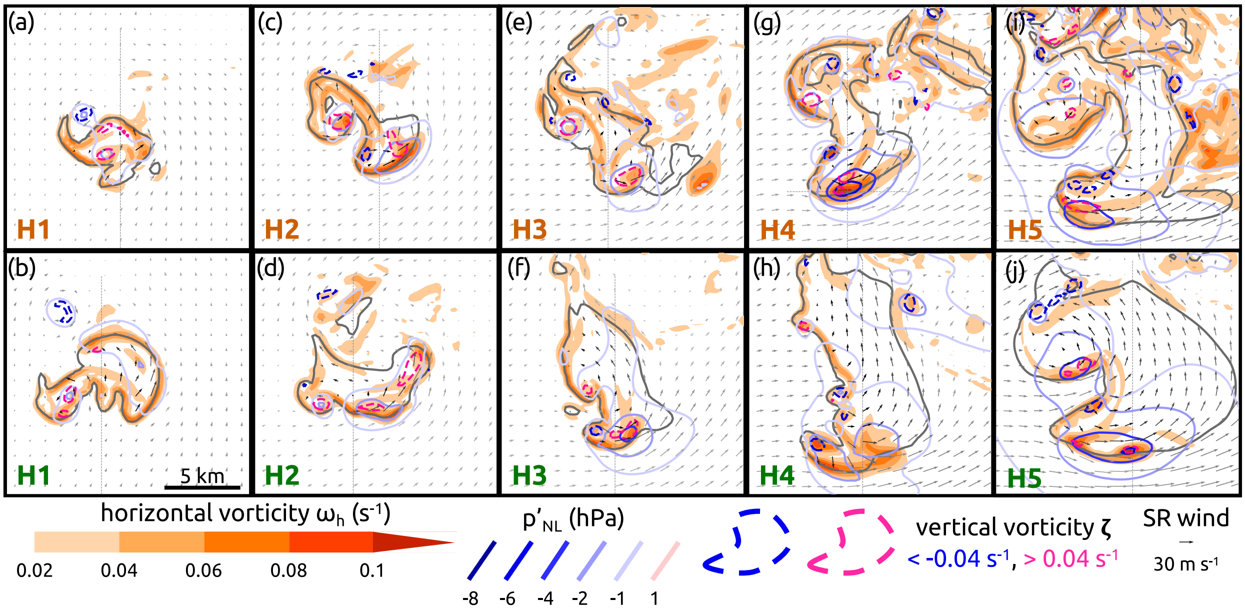

FIG. 6. As in Fig. 2, but showing horizontal vorticity (orange fill), nonlinear dynamic pressure perturbation (blue to red contours), and outlines of where vertical vorticity exceeds 0.04 s^{-1} (dashed pink contours) and is less than $-0.04\ s^{-1}$ (dashed blue contours).

Brought to you by NOAA Library | Unauthenticated | Downloaded 04/01/25 02:50 PM UTC

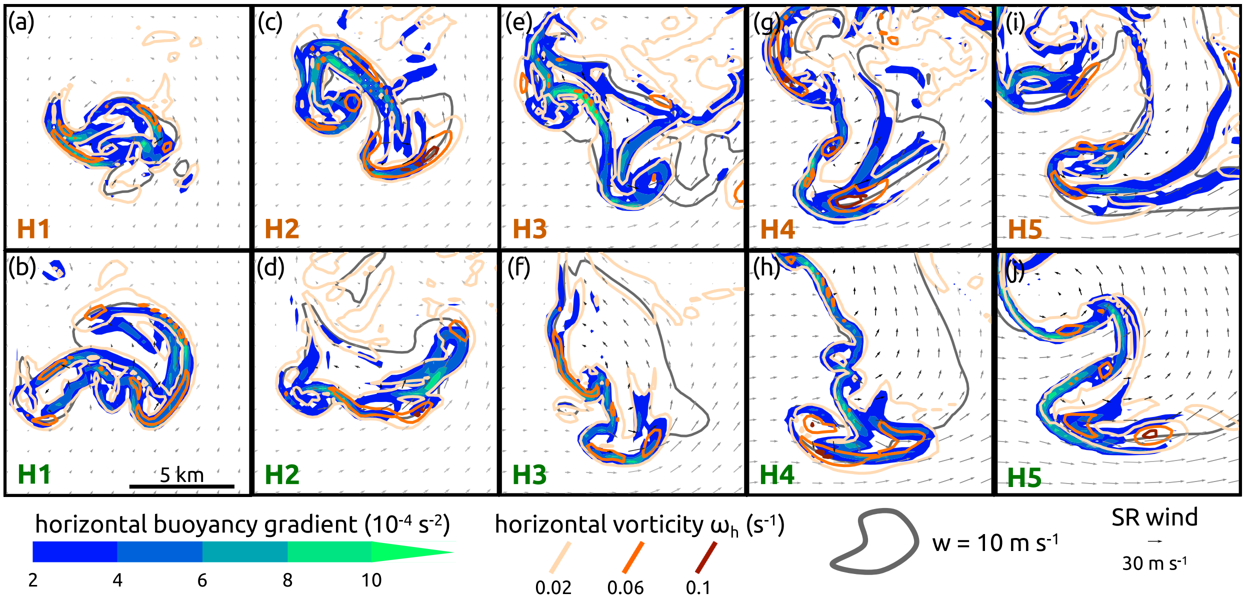

FIG. 7. As in Fig. 6, but plan views are 11.5 × 11.5 km^2 and shown is the horizontal gradient in buoyancy (cool fill), and horizontal vorticity contoured in orange at three values. Cross-sectional paths are omitted in this figure.

these findings, with large horizontal vorticity occurring almost exclusively along horizontal gradients in buoyancy (Fig. 7). We colloquially refer to these features as “horizontal rotors.” Regions of large horizontal vorticity can exist away from buoyancy gradients in the turbulent wake of the updraft (e.g., Fig. 7g), but this is to be expected given downstream advection via the midlevel storm-relative winds, which also explains the slight downstream displacement of the largest values of horizontal vorticity from the sharpest buoyancy gradients. Note that modifications to the local wind field due to the rotors themselves could alter the buoyancy distribution and associated gradients. Given our findings and those of the studies cited above, we are confident that horizontal rotors form primarily through baroclinic generation of vorticity, and we often refer to these features as “baroclinic vorticity.” As shown in Fig. 5, multiple horizontal rotors can exist simultaneously at different vertical levels on the updraft edge.

As seen in Fig. 6, localized regions of large vertical vorticity occur in conjunction with large horizontal vorticity. We attribute this, in addition to the tilting of midlevel environmental vorticity demonstrated in Fig. 4, to the tilting of baroclinic horizontal vorticity into the vertical. This process was analyzed by Damiani and Vali (2007), who observed that tilted toroidal circulations around cumulus clouds resulted in vertical vorticity of 0.04–0.1 s^{-1}. This tilting of baroclinic horizontal vorticity into the vertical is also shown by Lasher-Trapp et al. (2021, their Fig. 12), who found that horizontal rotors often contained a vertical component. Since baroclinic horizontal vorticity in horizontal rotors is very large in our simulations (often exceeding 0.1 s^{-1} per Figs. 5–7), even a slightly tilted horizontal rotor can result in large vertical vorticity.

A west–east vertical cross section through the southern edge of the H4-dry updraft (Fig. 8) affirms that horizontal rotors can indeed have substantial vertical tilt. As in the south–north cross sections (Fig. 5), negative p'_{NL} is well aligned with the horizontal rotor (the −4 hPa p'_{NL} contour exhibits very similar tilt with height as the rotor). As previously speculated, it can also be seen that the horizontal rotor has a pronounced effect on the nearby storm-relative winds, with enhanced flow into the updraft below it and enhanced flow out of the updraft above it. As noted in Fig. 6, the local vertical vorticity maximum is very well aligned with the horizontal rotor, occurring where the rotor is both strongest (in terms of horizontal vorticity) and most tilted, indicating that the tilt of horizontal rotors can lead to regions of large vertical vorticity (as in Damiani and Vali 2007).

Horizontal rotors are most common on the southern side of the updraft (e.g., Fig. 6). This is because the prevailing southwesterly to westerly midlevel SR flow is more aligned with flow in the southern part the updraft and less aligned with flow in the northern part, which, per Lasher-Trapp et al. (2021), maximizes stretching of horizontal vorticity. While horizontal wind vectors within the midlevel updraft are certainly not indicative of solid-body rotation (Fig. 2; as in Dahl 2017), general cyclonic curvature of flow within the updraft clearly contributes to this result as described in Lasher-Trapp et al. (2021). Given that the tilting of midlevel environmental vorticity and horizontal rotors both occur at the southern edge of the updraft (Figs. 4 and 8), these two processes are both partially responsible for the local maxima in vertical vorticity in this region, providing more reasoning for why vertical vorticity within the diluted updraft is often larger than that within the undiluted updraft (Fig. 2).

c. *Trends in horizontal rotor characteristics as low-level storm-relative flow and midlevel shear increase*

As LL SR flow increases (a result of altered storm motion associated with increased MLS), the minimum p'_{NL} within the

Brought to you by NOAA Library | Unauthenticated | Downloaded 04/01/25 02:50 PM UTC

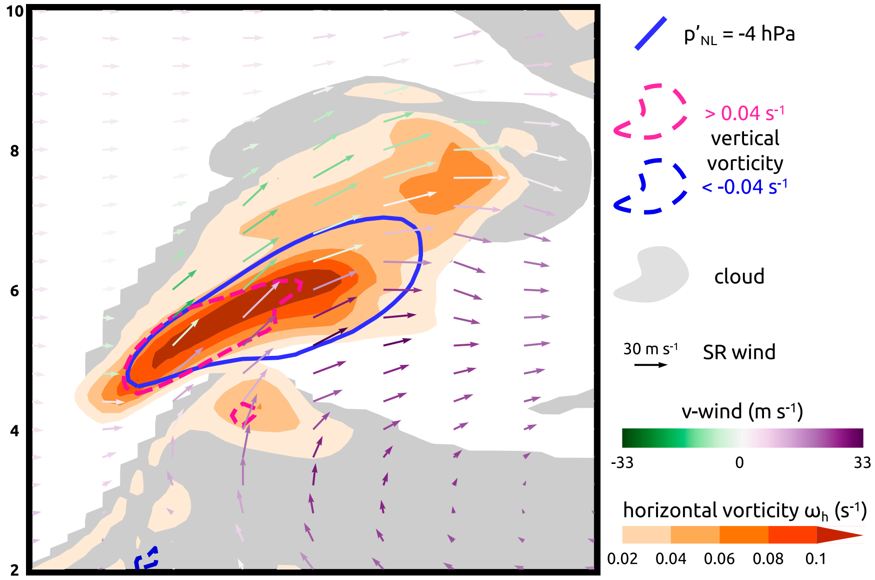

FIG. 8. West-to-east (left to right side of the figure) vertical cross section along the path through the H4-dry storm shown in Fig. 6g. Shown is cloud ($q_i + q_c > 0.0001$ g kg^{-1}; gray fill), horizontal vorticity (orange fill), outlines of where vertical vorticity exceeds (is less than) 0.04 s^{-1} (-0.04 s^{-1}; pink and blue dashed contours, respectively), where nonlinear dynamic pressure perturbation equals -4 hPa (blue contour), and storm-relative wind vectors (shaded green to purple by the speed and direction of the storm-relative v wind) every 400 m in the vertical and 1000 m in the horizontal. The cross section extends 8 km in the z direction and 8 km in the x direction. The z-axis labels are in kilometers.

horizontal rotors exhibits a pronounced, statistically significant decreasing trend (Fig. 9a). On average, the H5 storms contain horizontal rotors with p'_{NL} minima more than twice the magnitude of those in the H1 storms. Seeing that larger LL SR flow leads to wider midlevel updrafts (Fig. 9b), we initially speculated that larger buoyancy in these updrafts, independent of the magnitude of its horizontal gradient (Davies-Jones 2015), was leading to stronger horizontal rotors. Indeed, midlevel buoyancy is about 10% larger in the wider updrafts compared to the narrower updrafts (not shown), but other factors to be described in the following paragraphs also play roles in generating stronger horizontal rotors when LL SR flow is larger.

Another element leading to, on average, stronger horizontal rotors (as measured by their associated p'_{NL}) in the larger LL SR flow cases is the more steady-state nature of the updrafts. A transition from a thermal chain-like updraft structure to a plume-like updraft structure is known to occur once a certain updraft width threshold is reached (Morrison 2017; Peters et al. 2020a,c; Morrison et al. 2020), implying that storms in environments where LL SR flow exceeds a certain threshold are more steady state. This idea can be broadly applied to our simulations. In a relatively steady-state, plume-like updraft, fluctuations in updraft size at midlevels should be minimized compared to a narrower updraft consisting of individual "pulses" (e.g., compare Fig. 5a to Fig. 5j). The baroclinic generation of horizontal vorticity is maximized when the horizontal buoyancy gradient remains in the same updraft-relative position for as long as possible, giving parcels the longest residence time within the gradient, increasing the value resulting from an integration of the horizontal vorticity tendency equation with respect to time. This scenario is more likely to occur given a wider updraft, where fluctuations in midlevel updraft shape are minimized. Greater locational consistency of the horizontal rotor should be consistent with a stronger horizontal rotor, given that its location is strongly tied to the location of horizontal buoyancy gradients (Fig. 7).

Over the $t = 1$–2-h period, the H1-dry, H1-moist, and H2-dry storms (the storms with the weakest horizontal rotors) have much lower consistency in the updraft-relative location of the horizontal rotor (Fig. 9c). The maximum 5–7-km layer-averaged x component of horizontal vorticity along the updraft edge was used as the location of the horizontal rotor, and each time step was manually inspected to ensure this point was representative of the center of the rotor. The few times the maximum was not associated with a horizontal rotor (due to horizontal vorticity maxima that had been advected well downstream of the updraft), the maximum in horizontal vorticity at the updraft edge was manually assigned as the center location.

Excluding the H1-dry, H1-moist, and H2-dry cases, differences in the consistency of the location of the horizontal rotor show no trend as LL SR flow increases, possibly because each updraft now has a more plume-like, steady-state structure. This suggests that differences in updraft steadiness cannot explain the increase in horizontal rotor strength outside of the weakest storms.

As MLS increases, midlevel storm-relative winds become stronger and attain an increasing westerly component (Fig. 1).

Brought to you by NOAA Library | Unauthenticated | Downloaded 04/01/25 02:50 PM UTC

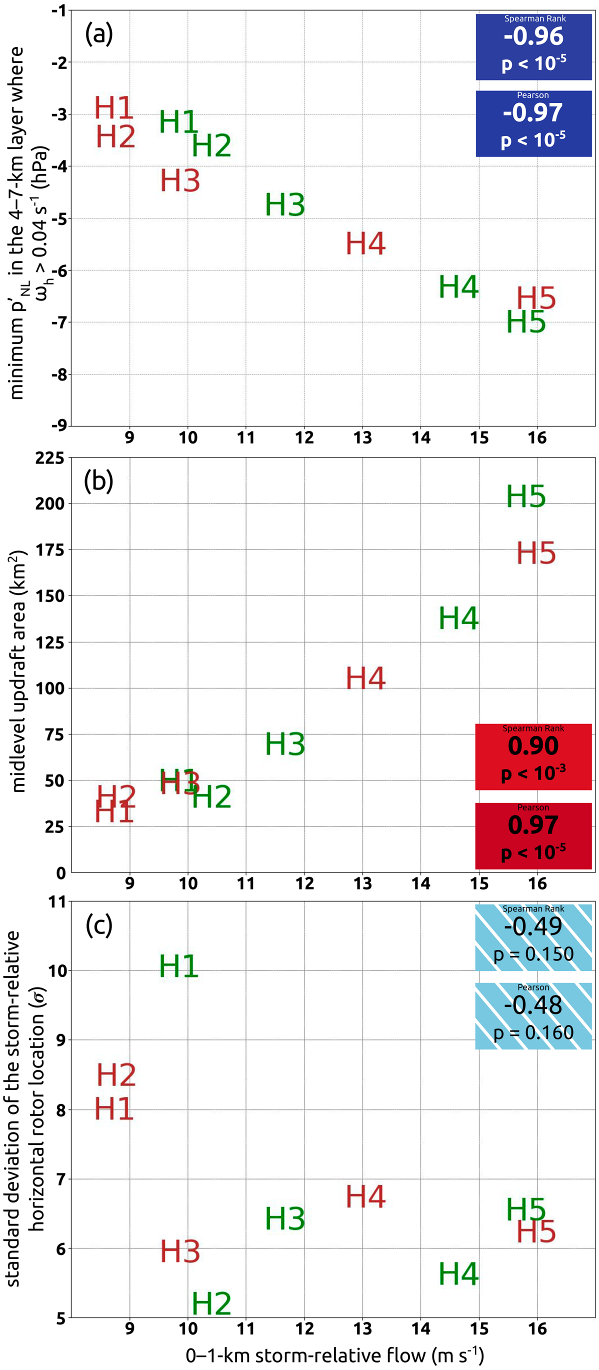

FIG. 9. The 0–1-km storm-relative flow calculated using the average simulated storm motion over $t = 1$–2 h vs (a) the minimum nonlinear dynamic pressure perturbation (hPa) in the 4–7-km layer where horizontal vorticity exceeds 0.04 s^{-1}, (b) horizontal area where 5–7-km layer-averaged vertical velocity exceeds 5 m s^{-1}, and (c) the standard deviation of the center of the horizontal rotor relative to the maximum 3–6-km layer-averaged vertical velocity. Brown (green) text indicates simulations with low (high) midlevel RH. All values are averaged over $t = 1$–2 h. The Pearson and Spearman rank correlation coefficients and p values are displayed as in Fig. 3.

This is visible near the bottom of the plan views in Fig. 7; 6-km storm-relative winds become stronger and more westerly from H1–H5. In general, the storm-relative wind vectors in Fig. 7 become more orthogonal to the horizontal buoyancy gradient at the southern edge of the updraft from H1–H5, which likely contributes to the increasing trend in rotor strength through increased generation of baroclinic vorticity owing to longer residence times within the gradient (e.g., Klemp and Rotunno 1983; Shabbott and Markowski 2006). There are still locations in the H1 and H2 simulations where midlevel SR flow is well aligned with the axis of a horizontal buoyancy gradient, but given the less steady-state nature of these updrafts, this alignment is likely rather transient.

The increase in horizontal rotor strength as shear increases is consistent with the findings of Jo and Lasher-Trapp (2022, 2023). Lasher-Trapp et al. (2021) and Jo and Lasher-Trapp (2022, 2023) argued that increased horizontal stretching along the southern edge of the midlevel updraft in environments with stronger midlevel storm-relative flow contributed to this trend, but horizontal stretching of vorticity does not systematically increase as midlevel SR flow increases in our simulations (not shown, likely due to similar midlevel mesocyclone strengths), meaning that it cannot explain the increase in rotor strength. We find the same result as Lasher-Trapp et al. (2021) and Jo and Lasher-Trapp (2022, 2023), but believe that it is explained by mechanisms that differ somewhat from their findings.

In summary, we suspect that the robust decrease in $p'_{\rm NL}$ associated with horizontal rotors as MLS and LL SR flow increase is a result of more buoyant, steady-state updrafts due to increased LL SR flow, and more westerly midlevel storm-relative flow that results from stronger midlevel winds required to increase MLS. A deeper, more rigorous investigation of the factors leading to the development of horizontal rotors and their comparative influence on rotor strength is omitted for the sake of brevity but is planned for a future study.

d. The dynamical impact of horizontal rotors

A consequence of large vorticity at the midlevel updraft edge, primarily associated with horizontal rotors (Figs. 5, 6, and 8) but also with tilted midlevel environmental vorticity (Fig. 4), is locally low nonlinear dynamic pressure. If the vertical gradient of this perturbation pressure is negative, an upward-directed acceleration occurs beneath the pressure minimum [Eq. (2)]. To assess changes in vertical accelerations related to different vorticity patterns and wind shear, we analyze the NLDPA and LDPA terms of Eq. (2).

In Fig. 10, LDPA (Figs. 10a–j) and NLDPA (Figs. 10k–t) averaged over the 0–6-km layer are shaded, with positive values in red (i.e., an upward-directed acceleration induced by locally low dynamic pressure aloft). As would be expected, LDPA exhibits a steady increasing trend in magnitude and spatial extent as MLS and LL SR flow increase (Figs. 10a–j). This is consistent with a stronger updraft-in-shear effect (Rotunno and Klemp 1982) as updraft width (Davies-Jones 2002) and shear increase, and suggests an increasing preference for upward vertical motion on the downshear flank of the updraft as

Brought to you by NOAA Library | Unauthenticated | Downloaded 04/01/25 02:50 PM UTC

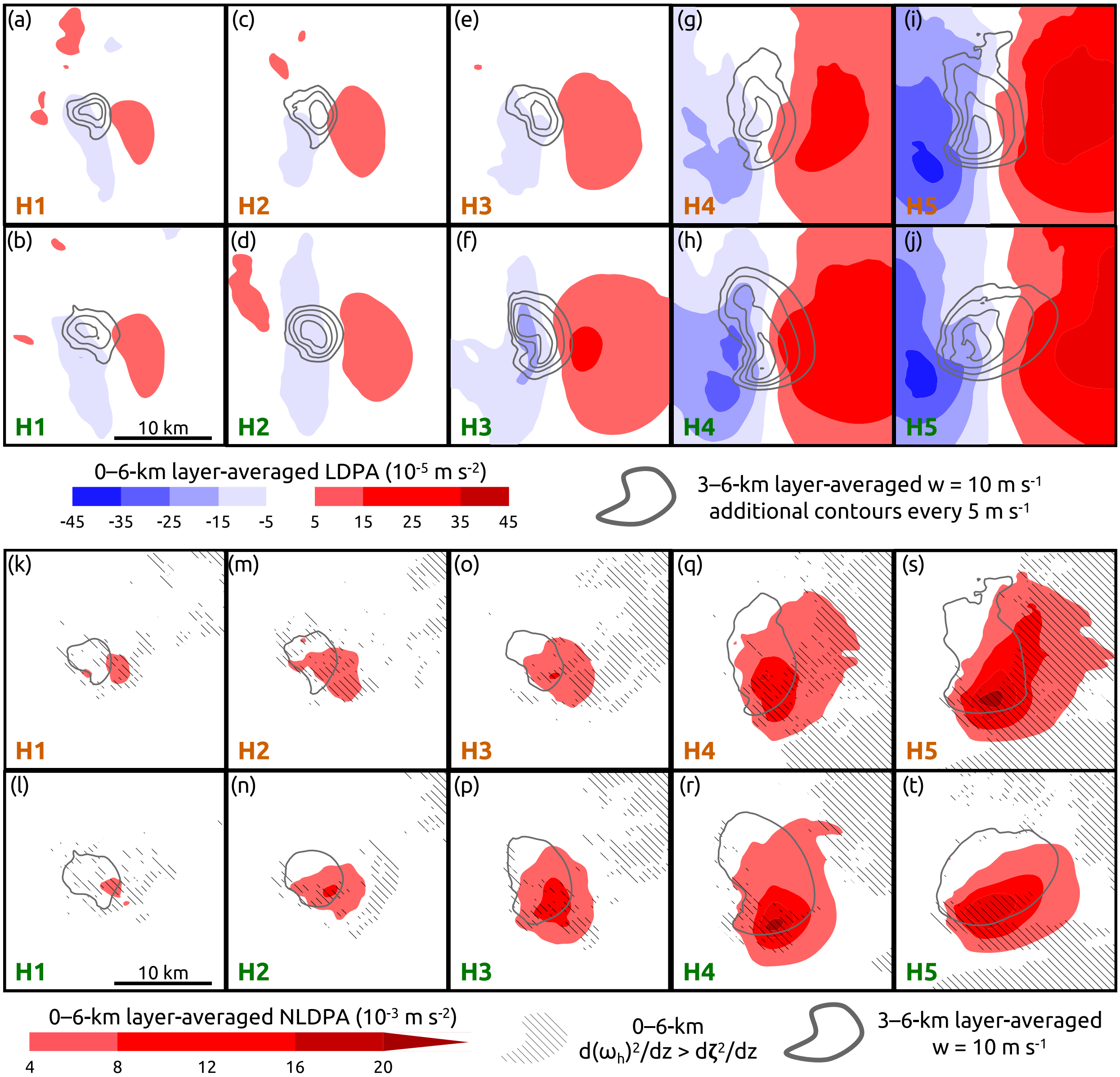

FIG. 10. 20 × 20 km^2 plan views of each storm, averaged over t = 1–2 h, showing 0–6-km layer-averaged (a)–(j) LDPA (blue to red fill) and (k)–(t) NLDPA (red fill), where 3–6-km layer-averaged vertical velocity equals 10 m s^{-1} [first gray contour, every additional 5 m s^{-1} in gray in (a)–(j)] where the vertical gradient in storm-modified horizontal vorticity is larger than the vertical gradient in vertical vorticity over the 0–6-km layer [in (k)–(t); black hatching] Note that the NLDPA magnitudes shaded are greater than one order of magnitude larger than that of LDPA.

shear increases. NLDPA also exhibits a steady increasing trend in magnitude and spatial extent as MLS and LL SR flow increase, with the greatest increase in magnitude focused on the southern and southeastern flanks of the midlevel updraft (Figs. 10k–t). NLDPA averaged over the 0–6-km layer is often more than an order of magnitude larger than that of LDPA [Fig. 10; Weisman and Rotunno (2000) also found LDPA to be much smaller than NLDPA in and around supercell updrafts]. Given the larger magnitude of NLDPA and its association with the horizontal rotor, the remainder of this section primarily focuses on the impacts of NLDPA on the updraft. It should be noted that the effective buoyancy pressure acceleration [EBPA, first term in Eq. (2)] also increases as MLS and LL SR flow increase (not shown), which is to be expected given the larger buoyancy in wider, less-diluted updrafts (Peters et al. 2019, 2020b; but theoretically only until a width allowing for an undiluted core is achieved; Jeevanjee and Romps 2016). This does lead to stronger updrafts via stronger vertical accelerations within the undiluted updraft core of EIL air (not shown), but has been well documented by recent

Brought to you by NOAA Library | Unauthenticated | Downloaded 04/01/25 02:50 PM UTC

studies, so we defer the reader to the previous citations for more information.

We believe that the increase in magnitude and spatial extent of NLDPA from H1–H5 (Figs. 10k–t) is primarily a result of decreasing $p'_{\rm NL}$ associated with horizontal rotors at midlevels (Fig. 9a). This is demonstrated in Figs. 10k–t. Since $p'_{\rm NL}$ depends strongly on the magnitude of storm-modified vorticity [Eq. (1)], its vertical gradient (i.e., NLDPA) also depends on the vertical gradient of storm-modified vorticity, which can be broken down into gradients of horizontal and vertical vorticity. The hatching in Figs. 10k–t indicates areas where the vertical gradient of the square of storm-modified horizontal vorticity is larger than that of vertical vorticity over the 0–6-km layer. In these regions, horizontal vorticity is contributing more to NLDPA over the 0–6-km layer than vertical vorticity. In each of the H4 and H5 cases, the maximum 0–6-km layer-averaged NLDPA occurs where the vertical gradient in horizontal vorticity is driving most of the vertical gradient in $p'_{\rm NL}$ (i.e., within the hatched regions). This suggests that horizontal vorticity associated with horizontal rotors is more important to midlevel updraft dynamics than vertical vorticity resulting from tilted midlevel environmental vorticity, at least during the t = 1–2-h period.

In addition to the collocation of NLDPA maxima where horizontal vorticity is driving low $p'_{\rm NL}$ at midlevels, the occurrence of NLDPA maxima near the southern edge of the midlevel updraft (particularly in the H3–H5 cases) suggests a comparatively minor dynamical influence of vertical vorticity associated with the midlevel mesocyclone within EIL-air. Later in this section, evidence will be shown that vertical vorticity within the mesocyclone is still the primary driver of *low-level* vertical accelerations. However, the above analysis underscores that horizontal rotors play a key role in driving 0–6-km layer-averaged NLDPA, which is also consistent with the fact that vertical vorticity often peaks well below 6 km AGL in supercell mesocyclones (McCaul and Weisman 1996; Skinner et al. 2014; Marquis et al. 2016).

In addition to increasing in magnitude, the location of maximum 0–6-km layer-averaged NLDPA shifts from the eastern flank of the midlevel updraft in the H1 storms to the southern flank in the H4 and H5 storms (Figs. 10k–t). Warren et al. (2017) found this same trend in their simulations as upper-level shear and LL SR flow increased (see their Fig. 13). They noted that the maximum NLDPA was "associated with a peak in midlevel vorticity" (Warren et al. 2017, p. 2672). Given our results, it seems likely that horizontal vorticity associated with horizontal rotors accounted for most of the peak in midlevel vorticity and was responsible for larger 0–6-km NLDPA in their simulations with larger LL SR flow. Again, the increase in vertical vorticity resulting from tilted midlevel environmental vorticity may partly explain this finding, but the trends described above are primarily the result of larger and stronger horizontal rotors when LL SR flow is larger (as shown in Figs. 9a and 10k–t). Similarly, Peters et al. (2020b) found a positive correlation between LL SR flow and NLDPA, particularly at midlevels (see their Fig. 14b), and speculated that this result could be partially explained by the tilting of larger above-EIL environmental vorticity typically present in large LL SR flow environments (since large LL SR flow often requires large shear above ~1 km). While tilted above-EIL environmental vorticity does slightly contribute to larger NLDPA when MLS is greater, the stronger horizontal rotors likely account for most of this result from Peters et al. (2020b).

The primarily nonlinear (Fig. 10) dynamic pressure accelerations associated with horizontal rotors have a pronounced influence on parcels that pass beneath them (Fig. 11). At t = 90 min during the H5-dry simulation, 4790 parcels were initialized every 500 m in the vertical and 1000 m in the horizontal within a box extending 20 km in the x direction, 17 km in the y direction, and 7 km in the z direction encompassing the southern half of the updraft, surrounding air, and much of the air to the west of the updraft. Parcels were integrated forward in time for 15 min using the model time step, and parcel data were output every 6 s.

Within a 36 s period centered on t = 99 min (9 min after parcel initialization), we identified 27 parcels that passed beneath the rotor (see the caption of Fig. 11). Parcels that participate in the EIL-driven updraft (Figs. 11a–c) during this period are analyzed separately from those that participate in an eastward extension of the updraft (Figs. 11d–f). A few parcels pass through the low-level updraft, are detrained, then enter the updraft again before passing beneath the rotor (Fig. 11a), resulting in a highly variable vertical velocity pattern for the first 8 min (Fig. 11b). Other parcels participating in the EIL-driven updraft when they pass beneath the horizontal rotor experience gradual ascent below 4 km AGL as buoyancy increases, until the "boost" from DPA beneath the horizontal rotor aids in greatly increasing the vertical velocity (by an average of 15 m s^{-1} from t = 98–100 min, Figs. 11b,c). After this, parcels are either detrained or continue to ascend through the upper levels of the updraft, and their vertical velocities decrease owing to strong downward-directed DPA, a result of downward-directed NLDPA above the $p'_{\rm NL}$ minimum associated with the horizontal rotor, as well as downward-directed LDPA, since p'_L is minimized at low to midlevels (where vertical wind shear is strongest, not shown).

Midlevel parcels that do not experience significant mixing with EIL-air (on average, the parcels analyzed in Figs. 11d–f attain a maximum EIL tracer concentration of less than 6%, not shown) within the updraft also experience a significant increase in vertical velocity as a result of DPA beneath the horizontal rotor. These parcels generally approach the southern edge of the updraft from the west with weak vertical velocity, but again experience a large positive vertical acceleration beginning just before t = 98 min. Rather than enhance preexisting positive vertical velocity, as is the case for parcels already residing in the updraft, DPA associated with the horizontal rotor generates a new region of vertical velocity. Most of these parcels achieve vertical velocities of 10–20 m s^{-1} and contribute to a region of large vertical velocity extending eastward from the southern side of the updraft (Fig. 11d). These regions of enhanced midlevel vertical velocity immediately downstream of the horizontal rotor are also visible in the H3-dry, H3-moist, and H4-dry simulations (Figs. 6e–g). After passing beneath the rotor, parcels continue to experience positive DPA (consistent with positive LDPA on the downshear

Brought to you by NOAA Library | Unauthenticated | Downloaded 04/01/25 02:50 PM UTC

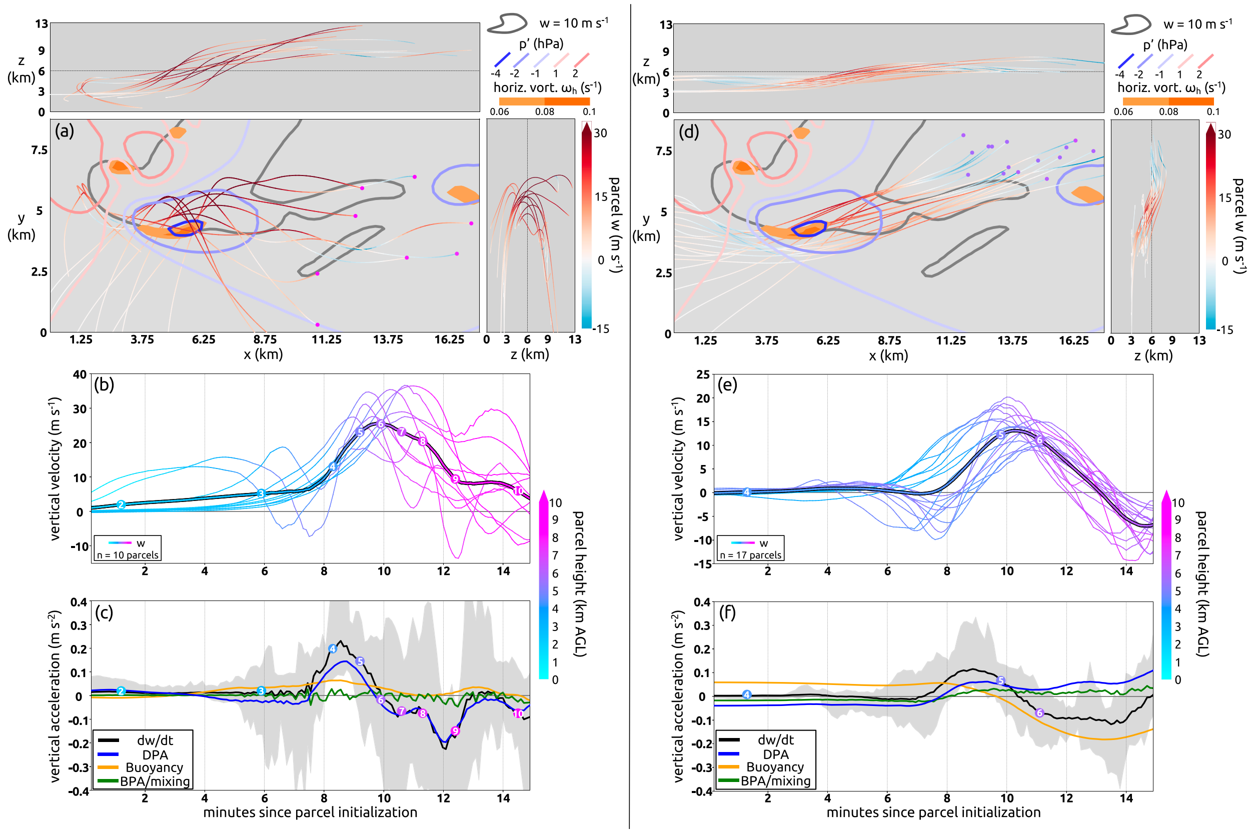

FIG. 11. Plan views of the H5-dry storm at $t = 99$ min showing 6-km horizontal vorticity (orange fill), where 6-km vertical velocity equals 10 m s^{-1} (gray contours), 6-km pressure perturbation (blue to red contours), and parcel trajectories over the 15-min integration period for (a) those that participate in the EIL-driven updraft and (d) those that participate in the rotor-induced updraft extension. Parcel trajectories appear on top of all fields if they exceed $z = 6$ km. Parcels were considered to participate in the EIL-driven updraft if they attained an EIL tracer concentration of more than 20% at any time or originated within the EIL. All parcels were required to pass through region extending from $x = 3.75$–6.75 km, $y = 3.25$–5.5 km, and $z = 4$–5.5 km, which is beneath the most intense portion of the horizontal rotor. The circles indicate parcel locations at $t = 105$ min and are colored by height [as in (b) and (e)]. (b),(e) Parcel vertical velocity along each trajectory, with lines colored by parcel height. Average vertical velocity is outlined in black. (c),(f) Average parcel vertical acceleration (black line; the region between the maximum and minimum is shaded gray), average parcel dynamic pressure acceleration (blue line), average parcel buoyancy (orange line), and average parcel acceleration due to anything but dynamic pressure acceleration and buoyancy (green line). Average parcel heights are indicated atop colored dots for each kilometer.

flank of the updraft in Fig. 10i), but its influence is outweighed by the development of strong negative buoyancy associated with adiabatic cooling, which leads to negative vertical velocity by $t = 105$ min.

For parcels that have substantially mixed with updraft air when passing beneath the rotor, DPA from $t = 97.7$–99.7 min contributes to an average increase in vertical velocity of 11.3 m s^{-1}, which is 62% of the total increase in vertical velocity over the same time period. For those that have not, DPA from $t = 98$–100 min contributes to an average increase in vertical velocity of 5.9 m s^{-1}, 52% of the total increase in vertical velocity over the same time period. Buoyancy accounts for 36% of the total increase in vertical velocity for the updraft parcels, and 39% for the nonupdraft parcels. This indicates that the rotor-induced acceleration works in tandem with, but is substantially larger than, the background state of positive buoyancy within and near the updraft.

e. A comparison of nonlinear dynamics in time

We now present an analysis of the H5-moist storm at two individual time steps. Throughout the $t = 1$–2-h period, differences in mesocyclone strength are rather small across the simulations (Figs. 2 and 3), and differences in midlevel vorticity-driven dynamics between storms are primarily caused by differences in the strength of horizontal rotors (Fig. 10). In the $t = 2$–3-h period, however, the H5-moist mesocyclone undergoes a period of pronounced strengthening, where an increase in vertical vorticity in the low-level mesocyclone leads to a groundward extension of the updraft and further intensification of low-level rotation (i.e., a "dynamical response"; Goldacker and Parker 2021), resulting in the most intense mesocyclone out of any simulation at any time.

In the H5-moist storm, the largest values of 0–6-km NLDPA are aligned with the horizontal rotor through at least $t = 2$ h

Brought to you by NOAA Library | Unauthenticated | Downloaded 04/01/25 02:50 PM UTC

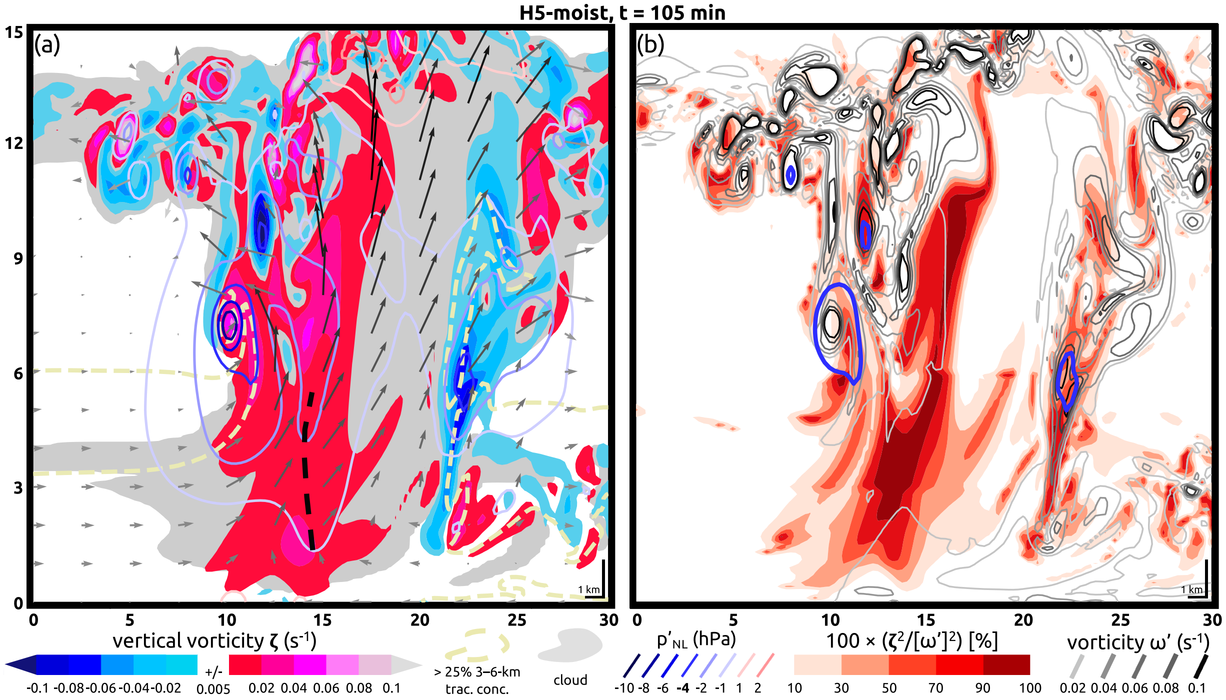

FIG. 12. South-to-north (left to right in each panel) vertical cross section through the center of the mesocyclone at $t = 105$ min for the H5-moist storm. (a) Cloud outline ($q_i + q_c > 0.0001$ g kg^{-1}; gray fill), vertical vorticity (red to blue fill), where 3–6-km tracer concentration exceeds 25% (dashed yellow contour), nonlinear dynamic pressure perturbation (blue and red contours), SR wind vectors plotted every 1 km in the vertical and 2.5 km in the horizontal, shaded by vertical velocity (darker arrows indicating larger vertical velocity), and the region of negative nonlinear dynamic pressure perturbation induced by the mesocyclone is indicated by the dashed black line near $y = 15$. (b) The ratio of vertical vorticity to total vorticity (orange to red fill), total storm-modified vorticity (gray contours), and nonlinear dynamic pressure perturbation contoured at −4 hPa (blue contours). Axes labels are in kilometers.

(Fig. 10t). A vertical cross section at $t = 105$ min (Fig. 12) provides additional context on why this occurs. At this time, p'_{NL} associated with the horizontal rotor (<9 hPa) is several times larger in magnitude than that associated with the midlevel mesocyclone (−1 to −3 hPa), even with vertical vorticity in the mesocyclone exceeding the common threshold of 0.005 s^{-1} (Davies-Jones 1984). Despite inducing a lesser magnitude of p'_{NL}, the mesocyclone results in a sharper vertical p'_{NL} gradient near the ground than the horizontal rotor, since its associated negative p'_{NL} extends to a lower level (Fig. 12a, see annotation). The opposite is true above 2 km: the vertical gradient of p'_{NL} associated with the horizontal rotor is much sharper than anywhere within the mesocyclone (Fig. 12a), further demonstrating why the maximum 0–6-km NLDPA occurs on the southern side of the H4 and H5 updrafts in Figs. 10g–j. Figure 12b affirms the role of horizontal vorticity in driving the midlevel p'_{NL} minimum. At the southern edge of the mid- to upper-level updraft, vorticity peaks at greater than 0.1 s^{-1}, and 70%–90%+ of its orientation is horizontal (note the lack of orange-red fill where vorticity is large). Meanwhile, the much weaker vorticity in the mesocyclone (<0.04 s^{-1}) is predominantly vertical.

This shows that there are different mechanisms for dynamic vertical forcing at different levels in the updraft. Even though the mesocyclone contains weaker vorticity than the horizontal rotor, it extends closer to the ground, inducing larger NLDPA in the 0–1-km layer (Fig. 13a, note that the southwestward extension of large NLDPA is partially facilitated by deformation-driven positive p'_{NL} near the surface associated with the gust front, visible at $y = 10$ in Fig. 12a). The horizontal rotor, which is denoted by the orange contour in Fig. 13a, has no correspondence with the region of maximum 0–1-km layer-averaged NLDPA, a feature more connected to the region of large 1-km vertical vorticity. Rather, the horizontal rotor, containing larger vorticity than the mesocyclone but confined to a shallower layer generally >4 km above the ground, induces a vertical acceleration above the lowest 1–2 km AGL that is reflected in the 1–6-km NLDPA field (Fig. 13b).

Regions where vertical vorticity is larger than horizontal vorticity at the minimum value of p'_{NL} within the 4–8-km layer are denoted by black hatching in Fig. 13b. Where 4–8-km p'_{NL} is at its lowest (−6 to −10 hPa), there is almost no hatching, suggesting that horizontal vorticity is, as expected, driving most of the low p'_{NL} in this layer, and therefore the large 1–6-km NLDPA beneath it. However, there is a narrow region where vertical vorticity is larger than horizontal vorticity at the 4–8-km p'_{NL} minima, and it is rather well aligned with the NLDPA maximum. Figure 12a (near $y = 11$) reveals that this region of enhanced vertical vorticity bears resemblance to the regions of tilted midlevel environmental vorticity in Fig. 4. Most of the low p'_{NL} above the NLDPA maximum is associated with horizontal

Brought to you by NOAA Library | Unauthenticated | Downloaded 04/01/25 02:50 PM UTC

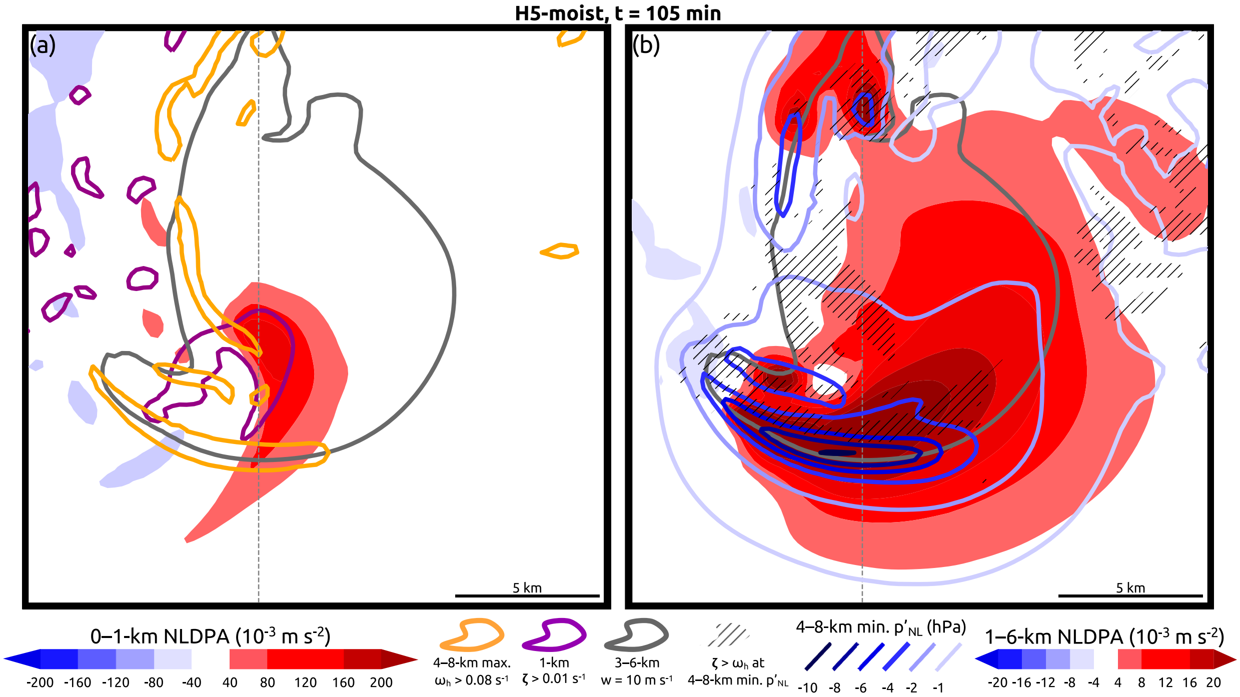

FIG. 13. 20 × 20 km^2 plan views for the H5-moist storm at t = 105 min. (a) The 0–1-km layer-averaged NLDPA (blue to red fill). Regions where the maximum horizontal vorticity in the 4–8-km layer exceeds 0.08 s^{-1} are outlined in orange. Areas where 1-km vertical vorticity exceeds 0.01 s^{-1} are outlined in purple. (b) The 1–6-km layer-averaged NLDPA [blue to red fill; note the change in magnitude from (a)]. Minimum nonlinear dynamic pressure in the 4–8-km layer is contoured in blue. Areas where vertical vorticity is larger than horizontal vorticity at the location of minimum 4–8-km nonlinear dynamic pressure perturbation are hatched in black. The gray contour indicates where 6-km vertical velocity equals 10 m s^{-1} in both plots, and the gray dashed line in both plots indicates the path of the cross section in Fig. 12.

vorticity (Fig. 13b), and the vertical vorticity of 0.02–0.04 s^{-1} responsible for the hatched region is much smaller than the predominantly horizontal vorticity exceeding 0.1 s^{-1} just to the south in the horizontal rotor (Fig. 12). Therefore, this does not challenge the finding that horizontal rotors are driving most of the low midlevel p'_{NL} and associated NLDPA, it merely highlights the comparatively small influence of tilted midlevel environmental vorticity on midlevel updraft dynamics.

By t = 170 min, the mesocyclone has strengthened considerably (Fig. 14a), with vertical vorticity exceeding 0.1 s^{-1}, several times larger than at t = 105 min. Accordingly, the minimum p'_{NL} within the mesocyclone has fallen to less than −15 hPa. Figure 14b indicates that, as expected, the large vorticity responsible for the development of low pressure within the mesocyclone is 60%–100% vertical. At the updraft edge, multiple horizontal rotors are still visible, but their associated p'_{NL} is now much smaller than that of the mesocyclone (the opposite of the case at t = 105 min). This suggests that the horizontal rotor's role in inducing vertical accelerations becomes overshadowed by that of the mesocyclone once vertical vorticity has increased to a certain point. Still, the magnitude of the p'_{NL} minimum associated with the horizontal rotor is the largest anywhere within the H5-moist storm until nearly two and a half hours into its life cycle, and the fact that most supercells never undergo such a pronounced increase in mesocyclone strength (Trapp et al. 2005; Goldacker and Parker 2021) suggests that the influence of the horizontal rotor on storm-scale vertical forcing is often significant.

At t = 170 min, the 1–6-km NLDPA field on the southern edge of the updraft is again dominated by the influence of the horizontal rotor (Fig. 15). At this time, however, the minimum 4–8-km p'_{NL} occurs in the center of the updraft where vertical vorticity dominates (Fig. 15b, although horizontal vorticity does appear to be responsible for a secondary p'_{NL} minimum near the center of the updraft). The northward tilt of the mesocyclone with height (evident in Fig. 14) results in a region of 1–6-km NLDPA similar in magnitude to that induced by the horizontal rotor, but the NLDPA induced by the horizontal rotor may be particularly important given that it induces a horizontal gradient in NLDPA that is directed to the southeast of the updraft center, which could influence storm motion. The 0–1-km NLDPA field, its maximum having increased by roughly one order of magnitude compared to t = 105 min, is clearly dominated by the low-level mesocyclone, again showing no connection to the horizontal rotor (Fig. 15a).

At both t = 105 min and t = 170 min, despite drastic differences in low-level mesocyclone strength, the largest 0–1-km NLDPA is associated with the low-level mesocyclone (Figs. 13a and 15a). Furthermore, 0–1-km NLDPA shows no connection to the horizontal rotor, and is generally much larger (1+ orders

Brought to you by NOAA Library | Unauthenticated | Downloaded 04/01/25 02:50 PM UTC

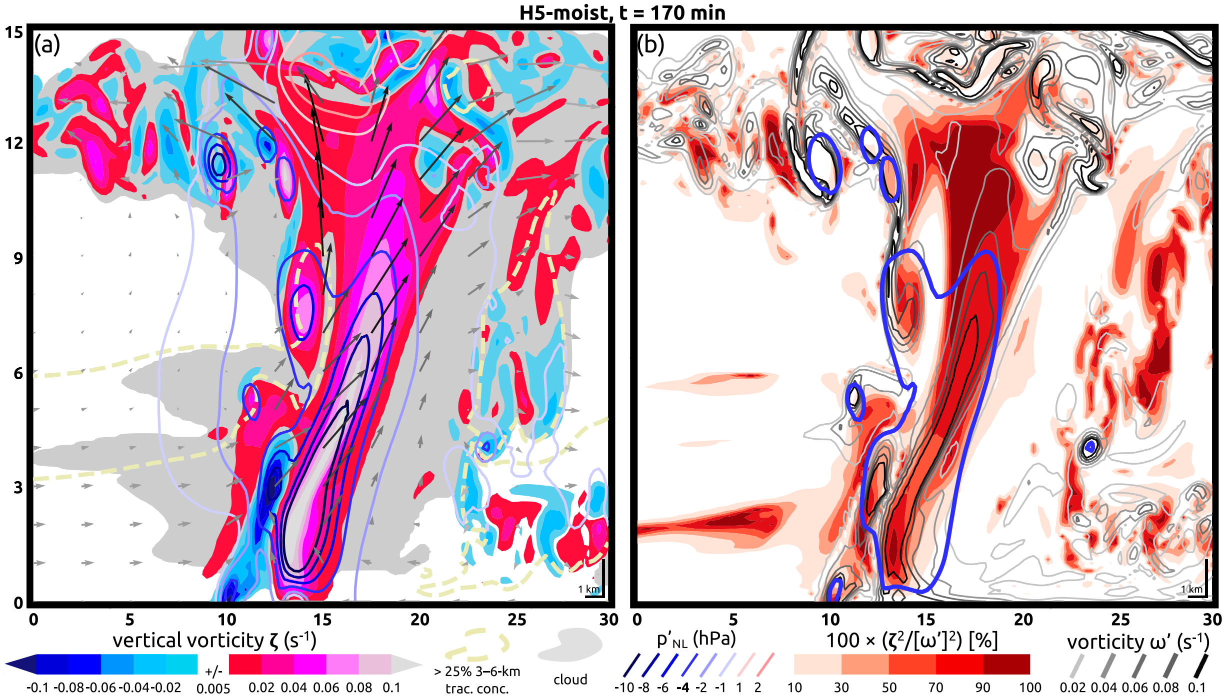

FIG. 14. As in Fig. 12, but for t = 170 min.

of magnitude) than 1–6-km NLDPA. This discrepancy in magnitude is partially a result of the larger depth (5 km) over which horizontal rotor-induced NLDPA was calculated, which can "wash out" the most intense regions of NLDPA associated with the relatively shallow, elevated horizontal rotor. In fact, the kilometer-deep layer below the center of the horizontal rotor for the H5-moist case at t = 105 min (Fig. 12a) experiences NLDPA on the order of that experienced in the kilometer-deep layer beneath the strong low-level mesocyclone at t = 170 min. This is implied by the sharp vertical gradient in p'_{NL} in the 6–7-km layer in Fig. 12a, but we chose not to show NLDPA for this layer since it resides well above the conditionally unstable EIL, and any relevance of this quantity at such an altitude to the storm remains ambiguous. However, as seen in Figs. 12a, 5f, 5g, and 5j, p'_{NL} of -1 hPa or less associated with horizontal rotors can extend into the upper reaches of the EIL (below 2800 m in our simulations). This suggests that horizontal rotors may be able to initiate ascent of CAPE-rich air at low levels.

This analysis of the H5-moist storm in time supports our impression that, in the 0–1-km layer, the acceleration induced by the horizontal rotor is negligible compared to the acceleration induced by the low-level mesocyclone, especially if the mesocyclone undergoes a pronounced increase in strength. While the first part of the preceding statement is intuitive, disentangling the location and magnitude of dynamical impacts from each of these large-vorticity features allows us to more confidently draw conclusions about the specific role that MLS and horizontal rotors play in supercell dynamics.

4. Discussion

We stress that the primary changes in updraft dynamics simulated herein as midlevel shear increases are not the result of increased environmental vorticity. The largest dynamical differences between storms simulated in environments with varied midlevel shear are related to horizontal rotors. Horizontal rotors appear to be connected to LL SR flow, a quantity indirectly related to midlevel shear. Changes in vertically oriented updraft rotation at midlevels, a quantity directly associated with the tilting of midlevel environmental vorticity inherent in midlevel shear, are small. Therefore, we argue that the most important effect of midlevel shear on a supercell is its control over LL SR flow. Midlevel shear influences the magnitude of vertical vorticity that results from the tilting of midlevel environmental vorticity at the updraft edge, which certainly plays a small role in generating low nonlinear dynamic pressure at midlevels, but is ultimately overshadowed by the dynamical influence of much larger *horizontal* vorticity within the horizontal rotor, a feature tied to updraft properties that are more connected to LL SR flow than midlevel environmental vorticity.

Operational forecasters have noted that a lack of midlevel shear is often associated with a lack of supercell "organization." The results herein suggest that the perceived lack of organization is not a result of small midlevel environmental vorticity, and is likely connected to other factors, such as small low-level SR flow that often accompanies weak midlevel shear.

There is likely a connection between horizontal rotors and storm motion. Though their calculations were not shown, Rotunno and Klemp (1982, 147–148, 1985) noted that horizontal

Brought to you by NOAA Library | Unauthenticated | Downloaded 04/01/25 02:50 PM UTC

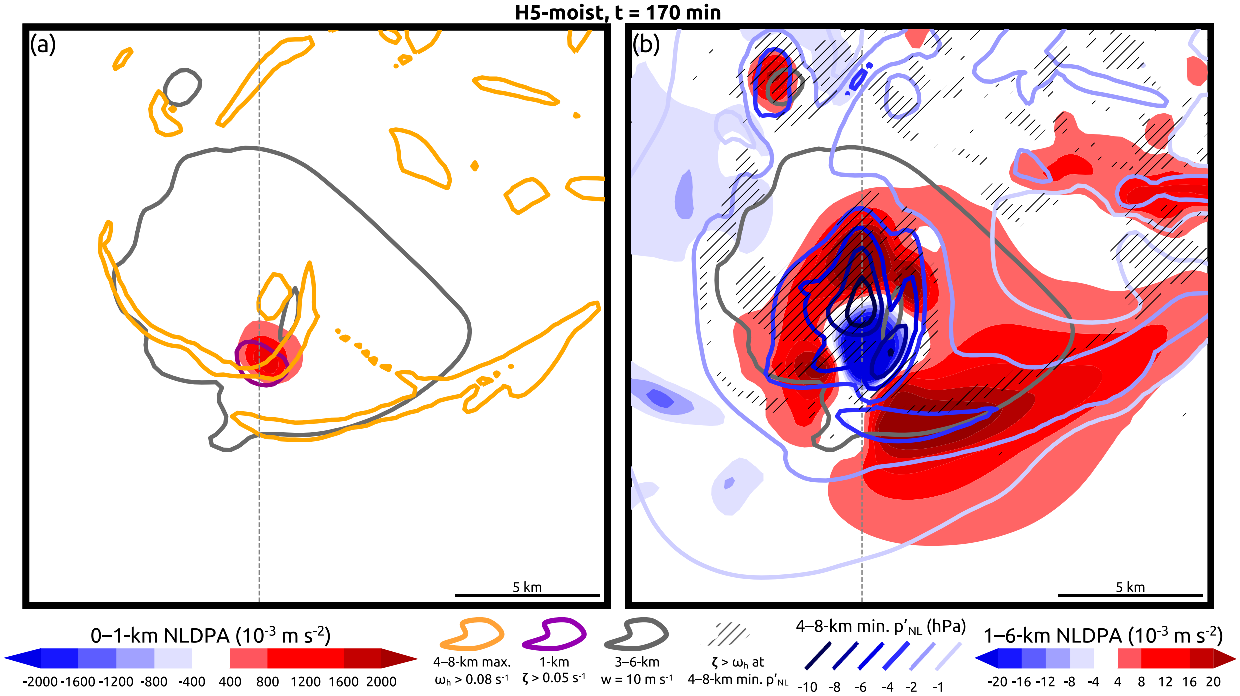

FIG. 15. As in Fig. 13, but at t = 170 min, and 1-km vertical vorticity in (a) is outlined at 0.05 s^{-1}. Note that the scale for 0–1-km layer-averaged NLDPA is an order of magnitude larger than in Fig. 13. The gray dashed line in both plots indicates the path of the cross section in Fig. 14.

vorticity associated with the horizontal buoyancy gradient at the updraft edge could induce a pressure perturbation exerting a comparable influence on storm splitting as that resulting from vertical vorticity. Cai and Wakimoto (2001) presented observational evidence that horizontal rotors play as large a role as vertical vorticity in the "rightward bias" of a supercell updraft, and the high resolution of our simulations and those of Lasher-Trapp et al. (2021) may mean that we are resolving these relatively small-scale horizontal rotors more clearly than previous simulations or radar observations.

It is possible that larger NLDPA associated with horizontal rotors on the updraft's southern flank leads to increased rightward, off-hodograph propagation, which is associated with increased tornado potential (Coniglio and Parker 2020; Flournoy et al. 2021). This could partially explain the results of Coniglio and Parker (2020) and Coniglio and Jewell (2022), who found LL SR flow to be significantly larger for tornadic compared to nontornadic supercells. Indeed, the H4 and H5 storms, relative to the predicted right-moving motion, move more to the right than the H1 and H2 storms (not shown). However, Davies-Jones (2002) showed that wider updrafts exhibit larger off-hodograph linear propagation. Therefore, it is unclear if this enhanced off-hodograph propagation is related solely to updraft width or dynamical effects of horizontal rotors in conjunction with updraft width. Additionally, the bulk of the acceleration induced by the rotor resides above the conditionally unstable EIL, subjecting its influence to further question. At the very least, lifting in association with the horizontal rotor could lead to near-field environmental modifications. Coniglio and Parker (2020, their Figs. 19d,e) showed that 1–3-km RH increased on approach to the southern flank of observed supercell updrafts, which may be at least partially attributable to ascent induced by horizontal rotors and resultant cooling. The influence of horizontal rotors on storm motion is currently being investigated.

The formation and controls on intensity of horizontal rotors is an open area of research. While increased low-level storm-relative flow leads to wider updrafts that are more buoyant and steady state at midlevels, typically resulting in stronger horizontal rotors, the influence of storm-relative flow at midlevels could be further investigated, given that it is known to impact storm evolution, structure [primarily upper-level storm-relative flow as in Rasmussen and Straka (1998)], and tornado production (Brooks et al. 1994; Gray and Frame 2021). In addition, storms in environments with low midlevel RH tended to have narrower midlevel updrafts (Fig. 9a). Given that LL SR flow and RH influence updraft width, which is well correlated with hydrometeor production (Grant and van den Heever 2014; Warren et al. 2017) and downdraft area (Marion and Trapp 2019), these results indicate that LL SR flow and free-tropospheric RH may be particularly relevant in determining where a supercell falls on the low-precipitation–classic-high-precipitation spectrum (e.g., large LL SR flow and high free-tropospheric RH may generally be more supportive of "high-precipitation" storms). Our simulated storms tended to have larger LL SR flow when midlevel RH was higher (Fig. 9; also seen in Bunkers et al. 2014),

Brought to you by NOAA Library | Unauthenticated | Downloaded 04/01/25 02:50 PM UTC

suggesting that free-tropospheric RH may influence low-level SR flow by impacting storm motion.

Pounds et al. (2024) observed that hailstones grow larger in the northeastern part of the midlevel updraft where cross-updraft flow is weaker owing to the diversion of southwesterly storm-relative flow around the updraft. Rotor-induced vertical accelerations may be relevant to hail production via alterations to updraft width and/or shape, since a change in updraft shape could modulate the size and location of the region favorable for hail growth. In other words, specific characteristics of horizontal rotors may represent a pathway by which increasing LL SR flow promotes larger hailstone growth. Future work should investigate how updraft shape is modulated by shear and horizontal rotors, and how this relates to hail production, as in Dennis and Kumjian (2017).

Doppler radar datasets (e.g., Van Den Broeke et al. 2023) may be particularly important in detecting horizontal rotors. Snyder et al. (2020) found evidence of an intense “quasi-horizontal vortex” as low as 1 km AGL in a supercell thunderstorm. Pressure retrieval as performed in Cai and Wakimoto (2001) would provide insight into the dynamics and influences of real-world horizontal rotors.

5. Conclusions

In this study, we provided an analysis of the influence of midlevel environmental vorticity associated with midlevel shear on supercell updrafts based on idealized numerical simulations. We also spent a considerable portion of our analysis evaluating the impact of regions of large storm-generated horizontal vorticity at midlevels, which we call horizontal rotors. Given our findings valid for the 10 simulations herein, we can answer our two questions about midlevel shear.

a. How does tilted midlevel environmental vorticity influence a supercell mesocyclone?

Cohesive updraft rotation does not exhibit a statistically significant trend with midlevel shear. However, the tilting of midlevel environmental vorticity does often lead to an area of large vertical vorticity on the southern edge of the midlevel updraft. The magnitude of this vertical vorticity can exceed that within EIL air in the center of the updraft (i.e., what we refer to as the “midlevel mesocyclone”) when midlevel shear is large, but does not lead to an increase in cohesive updraft rotation.

b. How does low-level storm-relative flow modulate the updraft and influence of tilted midlevel environmental vorticity?

Low-level storm-relative flow is related to updraft width. When midlevel shear is large, storm motions are faster relative to the low-level hodograph, low-level storm-relative flow is larger, and updrafts are wider. Midlevel air is kept from entering the cores of the wider updrafts, meaning that the only region where tilted midlevel environmental vorticity enhances vertical vorticity is the updraft edge.

The remaining conclusions relate to the horizontal rotor.

1) Updrafts in environments with larger midlevel shear and low-level storm-relative flow have a larger nonlinear dynamic pressure acceleration on their southern flank. This is primarily the result of stronger horizontal rotors at midlevels when updrafts are wider and midlevel storm-relative flow is more parallel to the southern edge of the updraft.
2) Horizontal vorticity associated with horizontal rotors is generally larger than that of vertical vorticity resulting from tilted low-level or midlevel environmental vorticity, and therefore plays a larger role in generating low pressure.
3) For most of a storm’s life cycle, the largest negative pressure perturbation at midlevels occurs in conjunction with the largest horizontal vorticity in the horizontal rotors, not vertical vorticity within the midlevel mesocyclone. This statement is reversed if the mesocyclone has undergone a pronounced increase in strength.
4) The vertical tilt of horizontal rotors leads to large vertical vorticity along the updraft edge, often larger than that within the mesocyclone.
5) The dynamic pressure acceleration resulting from low pressure within the horizontal rotor substantially enhances vertical velocity near the southern edge of the updraft and leads to a new region of rising air downstream of the rotor.
6) Regardless of the strength of the horizontal rotors and the mesocyclone, the strongest dynamic forcing in the lowest kilometer is driven by low pressure associated with vertical vorticity in the low-level mesocyclone, but the strongest dynamic forcing at the southern edge of the midlevel updraft is driven by horizontal rotors.

We emphasize that our conclusions are based on simulated, idealized supercells, and real-world results would likely be influenced by external forcing mechanisms not considered by the model such as storm mergers (Flournoy et al. 2022), terrain (Satrio et al. 2020; Katona and Markowski 2021), environmental inhomogeneities (Richardson et al. 2007; Nowotarski et al. 2014; Gray and Frame 2019; Brown et al. 2021), as well as more realistic microphysics (Murdzek et al. 2022), representation of Coriolis force, pressure gradient force, and convection initiation (Roberts et al. 2016; Markowski and Bryan 2016; Davies-Jones 2021), and different thermodynamic environments (McCaul and Weisman 2001; Kirkpatrick et al. 2009; Brown and Nowotarski 2019). Future modeling work should perform more realistic simulations and/or test the sensitivity of these results to different numerical designs. Continued storm-scale analyses of hundreds or thousands of observed supercell evolutionary traits (e.g., Gropp and Davenport 2018; Coniglio and Parker 2020; Davenport 2021; Flournoy et al. 2022; Lyza et al. 2022) will shed light on the relevance of these findings to real supercells and their hazards.

Acknowledgments. Funding was provided by NOAA/Office of Oceanic and Atmospheric Research under NOAA–University of Oklahoma Cooperative Agreement NA21OAR4320204, U.S.

Brought to you by NOAA Library | Unauthenticated | Downloaded 04/01/25 02:50 PM UTC

Department of Commerce. The statements, findings, conclusions, and recommendations are those of the authors and do not necessarily reflect the views of NOAA or the U.S. Department of Commerce. J. Peters's efforts were supported by National Science Foundation (NSF) Grants AGS-1928666, AGS-1841674, and the Department of Energy Atmospheric System Research (DOE ASR) Grant DE-SC0000246356. We thank three anonymous reviewers for thorough and thoughtful reviews of previous versions of this manuscript that greatly streamlined the revision process and led to this much improved version. We thank Drs. Mike Coniglio and Israel Jirak for internal reviews of this manuscript, and Dr. George Bryan for his continual support of CM1. All simulations were performed on NCAR's Cheyenne supercomputer (Computational and Information Systems Laboratory 2019).

Data availability statement. The namelist.input file, text files of the model soundings, and analysis code can be found at https://github.com/andrewtornado11/MLSResearch. CM1 can be downloaded from https://www2.mmm.ucar.edu/people/bryan/cm1/.

REFERENCES

Adlerman, E. J., K. K. Droegemeier, and R. Davies-Jones, 1999: A numerical simulation of cyclic mesocyclogenesis. *J. Atmos. Sci.*, **56**, 2045–2069, https://doi.org/10.1175/1520-0469(1999)056<2045:ANSOCM>2.0.CO;2.

Bentley, E. S., R. L. Thompson, B. R. Bowers, J. G. Gibbs, and S. E. Nelson, 2021: An analysis of 2016–18 tornadoes and National Weather Service tornado warnings across the contiguous United States. *Wea. Forecasting*, **36**, 1909–1924, https://doi.org/10.1175/WAF-D-20-0241.1.

Bluestein, H. B., and C. R. Parks, 1983: A synoptic and photographic climatology of low-precipitation severe thunderstorms in the Southern Plains. *Mon. Wea. Rev.*, **111**, 2034–2046, https://doi.org/10.1175/1520-0493(1983)111<2034:ASAPCO>2.0.CO;2.

——, and G. R. Woodall, 1990: Doppler-radar analysis of a low-precipitation severe storm. *Mon. Wea. Rev.*, **118**, 1640–1665, https://doi.org/10.1175/1520-0493(1990)118<1640:DRAOAL>2.0.CO;2.

Brandes, E. A., 1984: Relationships between radar-derived thermodynamic variables and tornadogenesis. *Mon. Wea. Rev.*, **112**, 1033–1052, https://doi.org/10.1175/1520-0493(1984)112<1033:RBRDTV>2.0.CO;2.

Brooks, H. E., C. A. Doswell III, and R. B. Wilhelmson, 1994: The role of midtropospheric winds in the evolution and maintenance of low-level mesocyclones. *Mon. Wea. Rev.*, **122**, 126–136, https://doi.org/10.1175/1520-0493(1994)122<0126:TROMWI>2.0.CO;2.

Brown, M. C., and C. J. Nowotarski, 2019: The influence of lifting condensation level on low-level outflow and rotation in simulated supercell thunderstorms. *J. Atmos. Sci.*, **76**, 1349–1372, https://doi.org/10.1175/JAS-D-18-0216.1.

——, ——, A. R. Dean, B. T. Smith, R. L. Thompson, and J. M. Peters, 2021: The early evening transition in southeastern U.S. tornado environments. *Wea. Forecasting*, **36**, 1431–1452, https://doi.org/10.1175/WAF-D-20-0191.1.

Browning, K. A., 1964: Airflow and precipitation trajectories within severe local storms which travel to the right of the winds. *J. Atmos. Sci.*, **21**, 634–639, https://doi.org/10.1175/1520-0469(1964)021<0634:AAPTWS>2.0.CO;2.

Bryan, G. H., and J. M. Fritsch, 2002: A benchmark simulation for moist nonhydrostatic numerical models. *Mon. Wea. Rev.*, **130**, 2917–2928, https://doi.org/10.1175/1520-0493(2002)130<2917:ABSFMN>2.0.CO;2.

Bunkers, M. J., B. A. Klimowski, J. W. Zeitler, R. L. Thompson, and M. L. Weisman, 2000: Predicting supercell motion using a new hodograph technique. *Wea. Forecasting*, **15**, 61–79, https://doi.org/10.1175/1520-0434(2000)015<0061:PSMUAN>2.0.CO;2.

——, D. A. Barber, R. L. Thompson, R. Edwards, and J. Garner, 2014: Choosing a universal mean wind for supercell motion prediction. *J. Oper. Meteor.*, **2**, 115–129, https://doi.org/10.15191/nwajom.2014.0211.

Cai, H., and R. M. Wakimoto, 2001: Retrieved pressure field and its influence on the propagation of a supercell thunderstorm. *Mon. Wea. Rev.*, **129**, 2695–2713, https://doi.org/10.1175/1520-0493(2001)129<2695:RPFAII>2.0.CO;2.

Coffer, B. E., and M. D. Parker, 2015: Impacts of increasing low-level shear on supercells during the early evening transition. *Mon. Wea. Rev.*, **143**, 1945–1969, https://doi.org/10.1175/MWR-D-14-00328.1.

——, and ——, 2017: Simulated supercells in nontornadic and tornadic VORTEX2 environments. *Mon. Wea. Rev.*, **145**, 149–180, https://doi.org/10.1175/MWR-D-16-0226.1.

——, ——, J. M. L. Dahl, L. J. Wicker, and A. J. Clark, 2017: Volatility of tornadogenesis: An ensemble of simulated nontornadic and tornadic supercells in VORTEX2 environments. *Mon. Wea. Rev.*, **145**, 4605–4625, https://doi.org/10.1175/MWR-D-17-0152.1.

Computational and Information Systems Laboratory, 2019: Cheyenne: HPE/SGI ICE XA System (University Community Computing). National Center for Atmospheric Research, https://doi.org/10.5065/D6RX99HX.

Coniglio, M. C., and M. D. Parker, 2020: Insights into supercells and their environments from three decades of targeted radiosonde observations. *Mon. Wea. Rev.*, **148**, 4893–4915, https://doi.org/10.1175/MWR-D-20-0105.1.

——, and R. E. Jewell, 2022: SPC mesoscale analysis compared to field-project soundings: Implications for supercell environment studies. *Mon. Wea. Rev.*, **150**, 567–588, https://doi.org/10.1175/MWR-D-21-0222.1.

Dahl, J. M. L., 2015: Near-ground rotation in simulated supercells: On the robustness of the baroclinic mechanism. *Mon. Wea. Rev.*, **143**, 4929–4942, https://doi.org/10.1175/MWR-D-15-0115.1.

——, 2017: Tilting of horizontal shear vorticity and the development of updraft rotation in supercell thunderstorms. *J. Atmos. Sci.*, **74**, 2997–3020, https://doi.org/10.1175/JAS-D-17-0091.1.

——, M. D. Parker, and L. J. Wicker, 2014: Imported and storm-generated near-ground vertical vorticity in a simulated supercell. *J. Atmos. Sci.*, **71**, 3027–3051, https://doi.org/10.1175/JAS-D-13-0123.1.

Damiani, R., and G. Vali, 2007: Evidence for tilted toroidal circulations in cumulus. *J. Atmos. Sci.*, **64**, 2045–2060, https://doi.org/10.1175/JAS3941.1.

Davenport, C. E., 2021: Environmental evolution of long-lived supercell thunderstorms in the Great Plains. *Wea. Forecasting*, **36**, 2187–2209, https://doi.org/10.1175/WAF-D-21-0042.1.

Davies-Jones, R., 1984: Streamwise vorticity: The origin of updraft rotation in supercell storms. *J. Atmos. Sci.*, **41**, 2991–3006,

Brought to you by NOAA Library | Unauthenticated | Downloaded 04/01/25 02:50 PM UTC

https://doi.org/10.1175/1520-0469(1984)041<2991:SVTOOU>2.0.CO;2.

——, 2002: Linear and nonlinear propagation of supercell storms. *J. Atmos. Sci.*, **59**, 3178–3205, https://doi.org/10.1175/1520-0469(2003)059<3178:LANPOS>2.0.CO;2.

——, 2003: An expression for effective buoyancy in surroundings with horizontal density gradients. *J. Atmos. Sci.*, **60**, 2922–2925, https://doi.org/10.1175/1520-0469(2003)060<2922:AEFEBI>2.0.CO;2.

——, 2015: A review of supercell and tornado dynamics. *Atmos. Res.*, **158–159**, 274–291, https://doi.org/10.1016/j.atmosres.2014.04.007.

——, 2021: Invented forces in supercell models. *J. Atmos. Sci.*, **78**, 2927–2939, https://doi.org/10.1175/JAS-D-21-0082.1.

——, 2022: Theory of parcel vorticity evolution in supercell-like flows. *J. Atmos. Sci.*, **79**, 1253–1270, https://doi.org/10.1175/JAS-D-21-0178.1.

——, D. W. Burgess, and M. Foster, 1990: Test of helicity as a forecast parameter. Preprints, *16th Conf. on Severe Local Storms*, Kananaskis Provincial Park, AB, Canada, Amer. Meteor. Soc., 588–592.

Dennis, E. J., and M. R. Kumjian, 2017: The impact of vertical wind shear on hail growth in simulated supercells. *J. Atmos. Sci.*, **74**, 641–663, https://doi.org/10.1175/JAS-D-16-0066.1.

de Rooy, W. C., and Coauthors, 2013: Entrainment and detrainment in cumulus convection: An overview. *Quart. J. Roy. Meteor. Soc.*, **139**, 1–19, https://doi.org/10.1002/qj.1959.

Dowell, D. C., and H. B. Bluestein, 2002: The 8 June 1995 McLean, Texas, storm. Part I: Observations of cyclic tornadogenesis. *Mon. Wea. Rev.*, **130**, 2626–2648, https://doi.org/10.1175/1520-0493(2002)130<2626:TJMTSP>2.0.CO;2.

Droegemeier, K. K., S. M. Lazarus, and R. Davies-Jones, 1993: The influence of helicity on numerically simulated convective storms. *Mon. Wea. Rev.*, **121**, 2005–2029, https://doi.org/10.1175/1520-0493(1993)121<2005:TIOHON>2.0.CO;2.

Emanuel, K. A., 1991: A scheme for representing cumulus convection in large-scale models. *J. Atmos. Sci.*, **48**, 2313–2329, https://doi.org/10.1175/1520-0469(1991)048<2313:ASFRCC>2.0.CO;2.

Flournoy, M. D., M. C. Coniglio, E. N. Rasmussen, J. C. Furtado, and B. E. Coffer, 2020: Modes of storm-scale variability and tornado potential in VORTEX2 near- and far-field tornadic environments. *Mon. Wea. Rev.*, **148**, 4185–4207, https://doi.org/10.1175/MWR-D-20-0147.1.

——, ——, and ——, 2021: Examining relationships between environmental conditions and supercell motion in time. *Wea. Forecasting*, **36**, 737–755, https://doi.org/10.1175/WAF-D-20-0192.1.

——, A. W. Lyza, M. A. Satrio, M. R. Diedrichsen, M. C. Coniglio, and S. Waugh, 2022: A climatology of cell mergers with supercells and their association with mesocyclone evolution. *Mon. Wea. Rev.*, **150**, 451–461, https://doi.org/10.1175/MWR-D-21-0204.1.

Gibbs, J. G., and B. R. Bowers, 2019: Techniques and thresholds of significance for using WSR-88D velocity data to anticipate significant tornadoes. *J. Oper. Meteor.*, **7**, 117–137, https://doi.org/10.15191/nwajom.2019.0709.

Gilmore, M. S., and L. J. Wicker, 1998: The influence of midtropospheric dryness on supercell morphology and evolution. *Mon. Wea. Rev.*, **126**, 943–958, https://doi.org/10.1175/1520-0493(1998)126<0943:TIOMDO>2.0.CO;2.

Goldacker, N. A., and M. D. Parker, 2021: Low-level updraft intensification in response to environmental wind profiles. *J. Atmos. Sci.*, **78**, 2763–2781, https://doi.org/10.1175/JAS-D-20-0354.1.

Grant, L. D., and S. C. van den Heever, 2014: Microphysical and dynamical characteristics of low-precipitation and classic supercells. *J. Atmos. Sci.*, **71**, 2604–2624, https://doi.org/10.1175/JAS-D-13-0261.1.

Gray, K., and J. Frame, 2019: Investigating the transition from elevated multicellular convection to surface-based supercells during the tornado outbreak of 24 August 2016 using a WRF Model simulation. *Wea. Forecasting*, **34**, 1051–1079, https://doi.org/10.1175/WAF-D-18-0209.1.

——, and ——, 2021: The impact of midlevel shear orientation on the longevity of and downdraft location and tornado-like vortex formation within simulated supercells. *Mon. Wea. Rev.*, **149**, 3739–3759, https://doi.org/10.1175/MWR-D-21-0085.1.

Gropp, M. E., and C. E. Davenport, 2018: The impact of the nocturnal transition on the lifetime and evolution of supercell thunderstorms in the Great Plains. *Wea. Forecasting*, **33**, 1045–1061, https://doi.org/10.1175/WAF-D-17-0150.1.

Guarriello, F., C. J. Nowotarski, and C. C. Epifanio, 2018: Effects of the low-level wind profile on outflow position and near-surface vertical vorticity in simulated supercell thunderstorms. *J. Atmos. Sci.*, **75**, 731–753, https://doi.org/10.1175/JAS-D-17-0174.1.

Hastings, R., and Y. Richardson, 2016: Long-term morphological changes in simulated supercells following mergers with nascent supercells in directionally varying shear. *Mon. Wea. Rev.*, **144**, 471–499, https://doi.org/10.1175/MWR-D-15-0193.1.

Hill, M. J. M., 1894: On a spherical vortex. *Philos. Trans. Roy. Soc.*, **A185**, 213–245, https://doi.org/10.1098/rsta.1894.0006.

James, R. P., and P. M. Markowski, 2010: A numerical investigation of the effects of dry air aloft on deep convection. *Mon. Wea. Rev.*, **138**, 140–161, https://doi.org/10.1175/2009MWR3018.1.

Jeevanjee, N., and D. M. Romps, 2016: Effective buoyancy at the surface and aloft. *Quart. J. Roy. Meteor. Soc.*, **142**, 811–820, https://doi.org/10.1002/qj.2683.

Jo, E., and S. Lasher-Trapp, 2022: Entrainment in a simulated supercell thunderstorm. Part II: The influence of vertical wind shear and general effects upon precipitation. *J. Atmos. Sci.*, **79**, 1429–1443, https://doi.org/10.1175/JAS-D-21-0289.1.

——, and ——, 2023: Entrainment in a simulated supercell thunderstorm. Part III: The influence of decreased environmental humidity and general effects upon precipitation efficiency. *J. Atmos. Sci.*, **80**, 1107–1122, https://doi.org/10.1175/JAS-D-22-0168.1.

Katona, B., and P. Markowski, 2021: Assessing the influence of complex terrain on severe convective environments in northeastern Alabama. *Wea. Forecasting*, **36**, 1003–1029, https://doi.org/10.1175/WAF-D-20-0136.1.

Kirkpatrick, C., E. W. McCaul Jr., and C. Cohen, 2009: Variability of updraft and downdraft characteristics in a large parameter space study of convective storms. *Mon. Wea. Rev.*, **137**, 1550–1561, https://doi.org/10.1175/2008MWR2703.1.

Klemp, J. B., and R. B. Wilhelmson, 1978: The simulation of three-dimensional convective storm dynamics. *J. Atmos. Sci.*, **35**, 1070–1096, https://doi.org/10.1175/1520-0469(1978)035<1070:TSOTDC>2.0.CO;2.

——, and R. Rotunno, 1983: A study of the tornadic region within a supercell thunderstorm. *J. Atmos. Sci.*, **40**, 359–377, https://doi.org/10.1175/1520-0469(1983)040<0359:ASOTTR>2.0.CO;2.

Lasher-Trapp, S., E. Jo, L. R. Allen, B. N. Engelsen, and R. J. Trapp, 2021: Entrainment in a simulated supercell thunderstorm. Part I: The evolution of different entrainment

Brought to you by NOAA Library | Unauthenticated | Downloaded 04/01/25 02:50 PM UTC

mechanisms and their dilutive effects. *J. Atmos. Sci.*, **78**, 2725–2740, https://doi.org/10.1175/JAS-D-20-0223.1.

LeBel, L. J., and P. M. Markowski, 2023: An analysis of the impact of vertical wind shear on convection initiation using large-eddy simulations: Importance of wake entrainment. *Mon. Wea. Rev.*, **151**, 1667–1688, https://doi.org/10.1175/MWR-D-22-0176.1.

Lebo, Z. J., and H. Morrison, 2015: Effects of horizontal and vertical grid spacing on mixing in simulated squall lines and implications for convective strength and structure. *Mon. Wea. Rev.*, **143**, 4355–4375, https://doi.org/10.1175/MWR-D-15-0154.1.

Lilly, D. K., 1986a: The structure, energetics and propagation of rotating convective storms. Part I: Energy exchange with the mean flow. *J. Atmos. Sci.*, **43**, 113–125, https://doi.org/10.1175/1520-0469(1986)043<0113:TSEAPO>2.0.CO;2.

——, 1986b: The structure, energetics and propagation of rotating convective storms. Part II: Helicity and storm stabilization. *J. Atmos. Sci.*, **43**, 126–140, https://doi.org/10.1175/1520-0469(1986)043<0126:TSEAPO>2.0.CO;2.

Lin, C., and A. Arakawa, 1997a: The macroscopic entrainment processes of simulated cumulus ensemble. Part I: Entrainment sources. *J. Atmos. Sci.*, **54**, 1027–1043, https://doi.org/10.1175/1520-0469(1997)054<1027:TMEPOS>2.0.CO;2.

——, and ——, 1997b: The macroscopic entrainment processes of simulated cumulus ensemble. Part II: Testing the entraining-plume model. *J. Atmos. Sci.*, **54**, 1044–1053, https://doi.org/10.1175/1520-0469(1997)054<1044:TMEPOS>2.0.CO;2.

Lyza, A. W., M. D. Flournoy, and E. N. Rasmussen, 2022: Observed characteristics of the tornadic supercells of 27–28 April 2011 in the southeast United States. *Mon. Wea. Rev.*, **150**, 2883–2910, https://doi.org/10.1175/MWR-D-21-0274.1.

Maddox, R. A., 1976: An evaluation of tornado proximity wind and stability data. *Mon. Wea. Rev.*, **104**, 133–142, https://doi.org/10.1175/1520-0493(1976)104<0133:AEOTPW>2.0.CO;2.

Marion, G. R., and R. J. Trapp, 2019: The dynamical coupling of convective updrafts, downdrafts, and cold pools in simulated supercell thunderstorms. *J. Geophys. Res. Atmos.*, **124**, 664–683, https://doi.org/10.1029/2018JD029055.

Markowski, P. M., 2020: What is the intrinsic predictability of tornadic supercell thunderstorms? *Mon. Wea. Rev.*, **148**, 3157–3180, https://doi.org/10.1175/MWR-D-20-0076.1.

——, and Y. Richardson, 2010: *Mesoscale Meteorology in Midlatitudes*. Wiley-Blackwell, 430 pp.

——, and ——, 2014: The influence of environmental low-level shear and cold pools on tornadogenesis: Insights from idealized simulations. *J. Atmos. Sci.*, **71**, 243–275, https://doi.org/10.1175/JAS-D-13-0159.1.

——, and G. H. Bryan, 2016: LES of laminar flow in the PBL: A potential problem for convective storm simulations. *Mon. Wea. Rev.*, **144**, 1841–1850, https://doi.org/10.1175/MWR-D-15-0439.1.

Marquis, J., Y. Richardson, P. Markowski, J. Wurman, K. Kosiba, and P. Robinson, 2016: An investigation of the Goshen County, Wyoming, tornadic supercell of 5 June 2009 using EnKF assimilation of mobile mesonet and radar observations collected during VORTEX2. Part II: Mesocyclone-scale processes affecting tornado formation, maintenance, and decay. *Mon. Wea. Rev.*, **144**, 3441–3463, https://doi.org/10.1175/MWR-D-15-0411.1.

McCaul, E. W., Jr., and M. L. Weisman, 1996: Simulations of shallow supercell storms in landfalling hurricane environments. *Mon. Wea. Rev.*, **124**, 408–429, https://doi.org/10.1175/1520-0493(1996)124<0408:SOSSSI>2.0.CO;2.

——, and ——, 2001: The sensitivity of simulated supercell structure and intensity to variations in the shapes of environmental buoyancy and shear profiles. *Mon. Wea. Rev.*, **129**, 664–687, https://doi.org/10.1175/1520-0493(2001)129<0664:TSOSSS>2.0.CO;2.

Morrison, H., 2016a: Impacts of updraft size and dimensionality on the perturbation pressure and vertical velocity in cumulus convection. Part I: Simple, generalized analytic solutions. *J. Atmos. Sci.*, **73**, 1441–1454, https://doi.org/10.1175/JAS-D-15-0040.1.

——, 2016b: Impacts of updraft size and dimensionality on the perturbation pressure and vertical velocity in cumulus convection. Part II: Comparison of theoretical and numerical solutions and fully dynamical simulations. *J. Atmos. Sci.*, **73**, 1455–1480, https://doi.org/10.1175/JAS-D-15-0041.1.

——, 2017: An analytic description of the structure and evolution of growing deep cumulus updrafts. *J. Atmos. Sci.*, **74**, 809–834, https://doi.org/10.1175/JAS-D-16-0234.1.

——, and J. M. Peters, 2018: Theoretical expressions for the ascent rate of moist deep convective thermals. *J. Atmos. Sci.*, **75**, 1699–1719, https://doi.org/10.1175/JAS-D-17-0295.1.

——, G. Thompson, and V. Tatarskii, 2009: Impact of cloud microphysics on the development of trailing stratiform precipitation in a simulated squall line: Comparison of one- and two-moment schemes. *Mon. Wea. Rev.*, **137**, 991–1007, https://doi.org/10.1175/2008MWR2556.1.

——, J. M. Peters, A. C. Varble, W. M. Hannah, and S. E. Giangrande, 2020: Thermal chains and entrainment in cumulus updrafts. Part I: Theoretical description. *J. Atmos. Sci.*, **77**, 3637–3660, https://doi.org/10.1175/JAS-D-19-0243.1.

——, ——, K. K. Chandrakar, and S. C. Sherwood, 2022: Influences of environmental relative humidity and horizontal scale of subcloud ascent on deep convective initiation. *J. Atmos. Sci.*, **79**, 337–359, https://doi.org/10.1175/JAS-D-21-0056.1.

Mulholland, J. P., J. M. Peters, and H. Morrison, 2021: How does vertical wind shear influence entrainment in squall lines? *J. Atmos. Sci.*, **76**, 1931–1946, https://doi.org/10.1175/JAS-D-20-0299.1.

Murdzek, S. S., P. M. Markowski, Y. P. Richardson, and R. L. Tanamachi, 2020: Processes preventing the development of a significant tornado in a Colorado supercell on 26 May 2010. *Mon. Wea. Rev.*, **148**, 1753–1778, https://doi.org/10.1175/MWR-D-19-0288.1.

——, Y. P. Richardson, P. M. Markowski, and M. R. Kumjian, 2022: How the environmental lifting condensation level affects the sensitivity of simulated convective storm cold pools to the microphysics parameterization. *Mon. Wea. Rev.*, **150**, 2527–2552, https://doi.org/10.1175/MWR-D-21-0258.1.

Nixon, C. J., and J. T. Allen, 2022: Distinguishing between hodographs of severe hail and tornadoes. *Wea. Forecasting*, **37**, 1761–1782, https://doi.org/10.1175/WAF-D-21-0136.1.

Nowotarski, C. J., P. M. Markowski, Y. P. Richardson, and G. H. Bryan, 2014: Properties of a simulated convective boundary layer in an idealized supercell thunderstorm environment. *Mon. Wea. Rev.*, **142**, 3955–3976, https://doi.org/10.1175/MWR-D-13-00349.1.

——, J. M. Peters, and J. P. Mulholland, 2020: Evaluating the effective inflow layer of simulated supercell updrafts. *Mon. Wea. Rev.*, **148**, 3507–3532, https://doi.org/10.1175/MWR-D-20-0013.1.

Orf, L., R. Wilhelmson, B. Lee, C. Finley, and A. Houston, 2017: Evolution of a long-track violent tornado within a simulated

Brought to you by NOAA Library | Unauthenticated | Downloaded 04/01/25 02:50 PM UTC

supercell. *Bull. Amer. Meteor. Soc.*, **98**, 45–68, https://doi.org/10.1175/BAMS-D-15-00073.1.

Parker, M. D., 2014: Composite VORTEX2 supercell environments from near-storm soundings. *Mon. Wea. Rev.*, **142**, 508–529, https://doi.org/10.1175/MWR-D-13-00167.1.

——, 2017: How much does "backing aloft" actually impact a supercell? *Wea. Forecasting*, **32**, 1937–1957, https://doi.org/10.1175/WAF-D-17-0064.1.

——, and R. H. Johnson, 2004: Structures and dynamics of quasi-2D mesoscale convective systems. *J. Atmos. Sci.*, **61**, 545–567, https://doi.org/10.1175/1520-0469(2004)061<0545:SADOQM>2.0.CO;2.

Peters, J. M., C. J. Nowotarski, and H. Morrison, 2019: The role of vertical wind shear in modulating maximum supercell updraft velocities. *J. Atmos. Sci.*, **76**, 3169–3189, https://doi.org/10.1175/JAS-D-19-0096.1.

——, H. Morrison, A. C. Varble, W. M. Hannah, and S. E. Giangrande, 2020a: Thermal chains and entrainment in cumulus updrafts. Part II: Analysis of idealized simulations. *J. Atmos. Sci.*, **77**, 3661–3681, https://doi.org/10.1175/JAS-D-19-0244.1.

——, C. J. Nowotarski, J. P. Mulholland, and R. L. Thompson, 2020b: The influences of effective inflow layer streamwise vorticity and storm-relative flow on supercell updraft properties. *J. Atmos. Sci.*, **77**, 3033–3057, https://doi.org/10.1175/JAS-D-19-0355.1.

——, ——, and G. L. Mullendore, 2020c: Are supercells resistant to entrainment because of their rotation? *J. Atmos. Sci.*, **77**, 1475–1495, https://doi.org/10.1175/JAS-D-19-0316.1.

——, J. P. Mulholland, and D. R. Chavas, 2022a: Generalized lapse rate formulas for use in entraining CAPE calculations. *J. Atmos. Sci.*, **79**, 815–836, https://doi.org/10.1175/JAS-D-21-0118.1.

——, H. Morrison, T. C. Nelson, J. N. Marquis, J. Mulholland, and C. J. Nowotarski, 2022b: The influence of shear on deep convection initiation. Part I: Theory. *J. Atmos. Sci.*, **79**, 1669–1690, https://doi.org/10.1175/JAS-D-21-0145.1.

——, ——, ——, ——, ——, and ——, 2022c: The influence of shear on deep convection initiation. Part II: Simulations. *J. Atmos. Sci.*, **79**, 1691–1711, https://doi.org/10.1175/JAS-D-21-0144.1.

——, B. E. Coffer, M. D. Parker, C. J. Nowotarski, J. P. Mulholland, C. J. Nixon, and J. T. Allen, 2023: Disentangling the influences of storm-relative flow and horizontal streamwise vorticity on low-level mesocyclones in supercells. *J. Atmos. Sci.*, **80**, 129–149, https://doi.org/10.1175/JAS-D-22-0114.1.

Pounds, L. E., C. L. Ziegler, R. D. Adams-Selin, and M. I. Biggerstaff, 2024: Analysis of hail production via simulated hailstone trajectories in the 29 May 2012 Kingfisher, Oklahoma, supercell. *Mon. Wea. Rev.*, https://doi.org/10.1175/MWR-D-23-0073.1, in press.

Rasmussen, E. N., and D. O. Blanchard, 1998: A baseline climatology of sounding-derived supercell and tornado forecast parameters. *Wea. Forecasting*, **13**, 1148–1164, https://doi.org/10.1175/1520-0434(1998)013<1148:ABCOSD>2.0.CO;2.

——, and J. M. Straka, 1998: Variations in supercell morphology. Part I: Observations of the role of upper-level storm-relative flow. *Mon. Wea. Rev.*, **126**, 2406–2421, https://doi.org/10.1175/1520-0493(1998)126<2406:VISMPI>2.0.CO;2.

Richardson, Y. P., K. K. Droegemeier, and R. P. Davies-Jones, 2007: The influence of horizontal environmental variability on numerically simulated convective storms. Part I: Variations in vertical shear. *Mon. Wea. Rev.*, **135**, 3429–3455, https://doi.org/10.1175/MWR3463.1.

Roberts, B., M. Xue, A. D. Schenkman, and D. T. Dawson, 2016: The role of surface drag in tornadogenesis within an idealized supercell simulation. *J. Atmos. Sci.*, **73**, 3371–3395, https://doi.org/10.1175/JAS-D-15-0332.1.

Romps, D. M., and Z. Kuang, 2010: Nature versus nurture in shallow convection. *J. Atmos. Sci.*, **67**, 1655–1666, https://doi.org/10.1175/2009JAS3307.1.

Rotunno, R., 1981: On the evolution of thunderstorm rotation. *Mon. Wea. Rev.*, **109**, 577–586, https://doi.org/10.1175/1520-0493(1981)109<0577:OTEOTR>2.0.CO;2.

——, and J. B. Klemp, 1982: The influence of the shear-induced pressure gradient on thunderstorm motion. *Mon. Wea. Rev.*, **110**, 136–151, https://doi.org/10.1175/1520-0493(1982)110<0136:TIOTSI>2.0.CO;2.

——, and J. Klemp, 1985: On the rotation and propagation of simulated supercell thunderstorms. *J. Atmos. Sci.*, **42**, 271–292, https://doi.org/10.1175/1520-0469(1985)042<0271:OTRAPO>2.0.CO;2.

——, and M. L. Weisman, 2003: Comment on "Linear and nonlinear propagation of supercell storms." *J. Atmos. Sci.*, **60**, 2413–2419, https://doi.org/10.1175/1520-0469(2003)060<2413:COLANP>2.0.CO;2.

Satrio, M. A., D. J. Bodine, A. E. Reinhart, T. Maruyama, and F. T. Lombardo, 2020: Understanding how complex terrain impacts tornado dynamics using a suite of high-resolution numerical simulations. *J. Atmos. Sci.*, **77**, 3277–3300, https://doi.org/10.1175/JAS-D-19-0321.1.

Schenkman, A. D., M. Xue, and M. Hu, 2014: Tornadogenesis in a high-resolution simulation of the 8 May 2003 Oklahoma City supercell. *J. Atmos. Sci.*, **71**, 130–154, https://doi.org/10.1175/JAS-D-13-073.1.

Shabbott, C. J., and P. M. Markowski, 2006: Surface in situ observations within the outflow of forward-flank downdrafts of supercell thunderstorms. *Mon. Wea. Rev.*, **134**, 1422–1441, https://doi.org/10.1175/MWR3131.1.

Skinner, P. S., C. C. Weiss, M. M. French, H. B. Bluestein, P. M. Markowski, and Y. P. Richardson, 2014: VORTEX2 observations of a low-level mesocyclone with multiple internal rear-flank downdraft momentum surges in the 18 May 2010 Dumas, Texas, supercell. *Mon. Wea. Rev.*, **142**, 2935–2960, https://doi.org/10.1175/MWR-D-13-00240.1.

Snyder, J. C., Z. B. Wienhoff, C. M. Kuster, and D. W. Reif, 2020: An analysis of an ostensible anticyclonic tornado from 9 May 2016 using high-resolution, rapid-scan radar data. *Wea. Forecasting*, **35**, 1685–1712, https://doi.org/10.1175/WAF-D-20-0055.1.

Thompson, R. L., C. M. Mead, and R. Edwards, 2007: Effective storm-relative helicity and bulk shear in supercell thunderstorm environments. *Wea. Forecasting*, **22**, 102–115, https://doi.org/10.1175/WAF969.1.

Trapp, R. J., G. J. Stumpf, and K. L. Manross, 2005: A reassessment of the percentage of tornadic mesocyclones. *Wea. Forecasting*, **20**, 680–687, https://doi.org/10.1175/WAF864.1.

Van Den Broeke, M. S., M. B. Wilson, C. A. Van Den Broeke, D. J. Healey, M. J. Wood, and R. E. Nelson, 2023: Polarimetric radar observations of a long-lived supercell and associated tornadoes on 10–11 December 2021. *Mon. Wea. Rev.*, **151**, 2501–2520, https://doi.org/10.1175/MWR-D-22-0330.1.

Warren, R. A., H. Richter, H. A. Ramsay, S. T. Siems, and M. J. Manton, 2017: Impact of variations in upper-level shear on

Brought to you by NOAA Library | Unauthenticated | Downloaded 04/01/25 02:50 PM UTC

simulated supercells. *Mon. Wea. Rev.*, **145**, 2659–2681, https://doi.org/10.1175/MWR-D-16-0412.1.

——, ——, and R. L. Thompson, 2021: Spectrum of near-storm environments for significant severe right-moving supercells in the contiguous United States. *Mon. Wea. Rev.*, **149**, 3299–3323, https://doi.org/10.1175/MWR-D-21-0006.1.

Weisman, M. L., and R. Rotunno, 2000: The use of vertical wind shear versus helicity in interpreting supercell dynamics. *J. Atmos. Sci.*, **57**, 1452–1472, https://doi.org/10.1175/1520-0469(2000)057<1452:TUOVWS>2.0.CO;2.

Wicker, L. J., and R. B. Wilhelmson, 1995: Simulation and analysis of tornado development and decay within a three-dimensional supercell thunderstorm. *J. Atmos. Sci.*, **52**, 2675–2703, https://doi.org/10.1175/1520-0469(1995)052<2675:SAAOTD>2.0.CO;2.

Zipser, E. J., 2003: Some views on "hot towers" after 50 years of tropical field programs and two years of TRMM data. *Cloud Systems, Hurricanes, and the Tropical Rainfall Measuring Mission (TRMM)*, *Meteor. Monogr.*, No. 29, Amer. Meteor. Soc., 49–58, https://doi.org/10.1175/0065-9401(2003)029<0049:CSVOHT>2.0.CO;2.

Brought to you by NOAA Library | Unauthenticated | Downloaded 04/01/25 02:50 PM UTC